Integrated RF/Optical Ground Station Technology Challenges

Daniel Hoppe,* Jeff Charles,† Sabino Piazzolla,† Farid Amoozegar,†
Mike Britcliffe,* and Hamid Hemmati†

Deep-space optical communication, which can provide a high-capacity downlink, is planned for future Deep Space Network (DSN) operations. It is envisioned that in addition to this new capability, RF communications will continue to be used for standard-capacity downlink and uplink. Since both links will exist in the future DSN, it is natural to ask whether the two ground stations might be combined into a single unit to result in cost benefits. Further, significant operational and cost benefits can result from a simple co-location of the RF and optical facilities at the existing DSN sites. These same benefits apply whether the RF and optical ground stations are combined or remain separated but co-located. There are a number of significant and unique technical challenges that must be addressed in the design of a combined RF and optical ground terminal. These are related to the coexistence of RF and optical surfaces, the impact of the optical components on the very-high-performance RF system, and RF/optical signal separation. Operation of the optical terminal without a radome implies technical challenges in terms of mirror materials, cleanliness, and stray radiation. Structural deformations of the antenna, which are nearly negligible for the RF signal, are significant for the optical system and must be addressed. This article describes recent work in assessing and addressing the technical challenges associated with a combined RF/optical ground station.

I. Introduction

Deep-space optical communication, which can provide a high-capacity downlink, is planned for future Deep Space Network (DSN) operations [1]. It is envisioned that in addition to this new capability, RF communications will continue to be used for standard-capacity downlink and uplink. Since both links will exist in the future DSN, it is natural to ask whether the two ground stations might be combined into a single unit to result in cost benefits. In addition, since the optical collection area is expected to encompass around 10 m in diameter, or less than 10 percent of the RF collection area of a 34-m-diameter antenna, it is conceivable that the optical area's affect on the RF performance could be minimized. Further, significant operational and cost benefits can result from a simple co-location of the

---

RF and optical facilities at the existing DSN sites. These same benefits apply whether the RF and optical ground stations are combined or remain separated but co-located.

There are a number of significant and unique technical challenges that must be addressed in the design of a combined RF and optical ground terminal. These are related to the coexistence of RF and optical surfaces, the impact of the optical components on the very-high-performance RF system, and RF/optical signal separation. Operation of the optical terminal without a radome implies technical challenges in terms of mirror materials, cleanliness, and stray radiation. Structural deformations of the antenna, which are nearly negligible for the RF signal, are significant for the optical system and must be addressed. Finally, the characterization of the Goldstone Deep Space Communications Complex as an optical communications site is essential for proper design of the terminal. Here we describe recent work done in these areas, form conclusions, and discuss future work.

II. General Optical Design Approaches

Reception of communication by an optical ground terminal does not require the optical quality of an astronomical telescope, but it does require resolution considerably better than, for example, that of a solar collector. This is driven by the fact that most deep-space optical communication opportunities will actually occur when the Earth optical ground terminal is in daylight. Thus, the field of view on the daytime sky must be limited in order to facilitate detection of the relatively dim optical communication signal. Three strawman concepts for the combined terminal are currently under consideration. Two of these take a conservative approach, based largely on existing ground station assumptions in terms of field of view and collection area. Of these, one is a shared-aperture approach where a portion of the primary and secondary surfaces is shared by the optical and RF beams. The second inserts an array of independent telescope apertures in the RF primary and sums the signals for these separate apertures. In this concept, the optical collection area is not illuminated by the RF beam. A third, less conservative approach, uses a shared aperture based on more RF-like metal panels, and trades a larger field of view for more, but less expensive, collecting area.

Current stand-alone optical ground station designs require that the angular size of the spot formed of a distant point source object by the optical terminal must fit onto a communication detector array having an angular field of view no larger 50 μrad, or approximately 10 arcsec. Budgeting for other sources of degradation, this generally implies that the maximum spot size due to the optics should not exceed 10 or 20 μrad. This requires an optical surface and alignment accuracy that is perhaps only 10 to 20 times less stringent than what is required for an astronomical imaging telescope. Given the above field of view, it is envisioned that, to obtain anticipated downlink data rates, the receive aperture (single or arrayed) will need to have an optical collecting area equivalent to a 10-m-diameter circular aperture. Since a typical 10-m-class optical telescope is relatively expensive, optical approaches having lower implementation costs than such telescopes have been pursued, particularly in the case of the shared-aperture strawman concept.

As mentioned above, the third approach — large field of view, large collecting area — aims to polish the existing RF surfaces to minimize scattered light effects and accept the exist-

ing surface distortions and thermal effects associated with the aluminum panels. These defects will produce a relatively large optical spot in the focal plane, which is collected using a much larger detector. The large detector also implies the system will collect more background light as well.

Any optical design must account for the distortion of the structure as the antenna points to different areas of the sky, the difference in optical refraction between the RF and optical beams, and the blurring due to atmospheric turbulence. The first two effects can be handled through the use of a fine-steering mirror system in the optical path or a larger detector, while the atmospheric effects must be accommodated by the detector size. All of these items are discussed in subsequent sections of this article.

III. Impact of the Optical Components on the RF Performance

The primary figure of merit for the RF link and antenna performance is the ratio of antenna gain (G), or collection area to noise temperature (T). This figure of merit, G/T, determines the signal-to-noise ratio of the link. Gain is mainly a function of collecting area, including the effects of surface reflectivity, surface errors, and coupling of the incident energy into the RF feedhorn, which directs the energy to the low-noise amplifier. Deep-space RF links are possible to a large extent because of the low-noise environment presented by the 3-K cosmic background. The noise temperature impact of the antenna is mainly affected by the 300-K Earth environment scattered into beam-through spillover past the primary, reflections off various support structures, and leakage through the panel gaps on the primary. Thermal noise is also added whenever the RF beam encounters a component with nonzero dissipation. The noise added is approximately equal to the physical temperature of the component times its absorption. Care must be taken when optical components are added to the RF system to avoid introducing new scatters that give more visibility of the 300-K environment or add additional loss in the RF path.

The RF figure of merit, G/T, is typically more sensitive to T than G. For example, a typical DSN 34-m antenna presents a total system noise temperature of approximately 30 K. If 9 percent (80 m^2) of the primary antenna surface were left open or allowed to view the ambient environment, the system would experience an increase in system temperature of 27 K. This represents a decrease in G/T of approximately 3 dB, whereas the loss in surface area represents a loss on the order of 0.4 dB. Thus, extreme care must be exercised with respect to controlling additional noise introduced into the RF system due to the addition of the optical capability.

IV. RF/Optical Signal Separation

One of the most critical items in the RF/optical chain is a device for separating the RF and optical beams. The shared-aperture strawman design calls for a beam splitter that is embedded in a larger RF mirror in the beam-waveguide path, as depicted in Figure 1. Ideally, the splitter should reflect the RF beam with better than 95 percent efficiency, while the laser
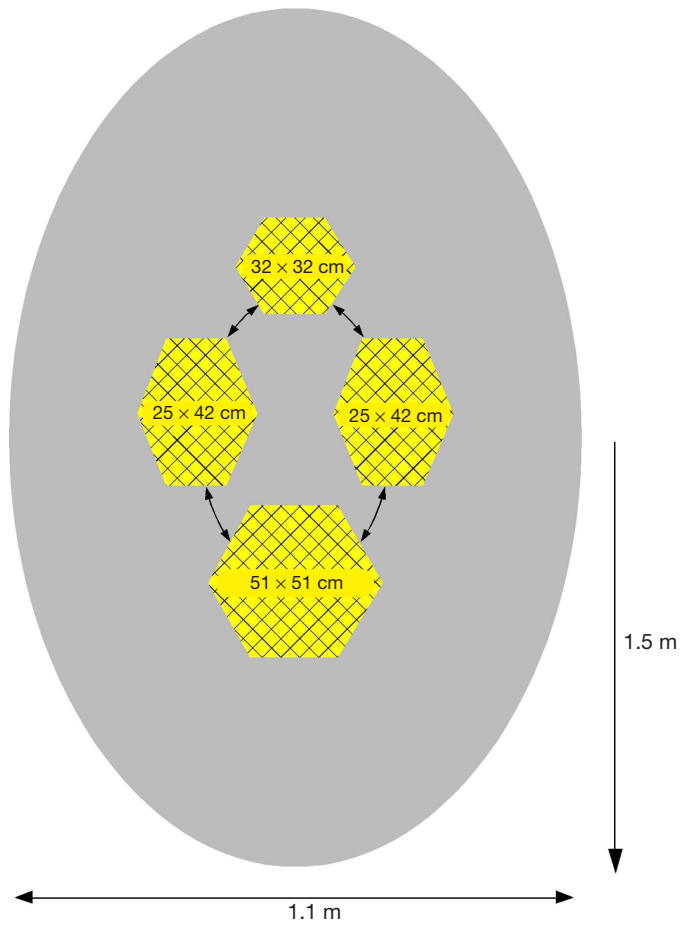
Figure 1. RF/optical beam splitter (front view).

signal at 1550 nm must be transmitted through the component with better than 90 percent efficiency. The RF reflectivity is sized to limit the noise temperature increase due to the separator to 2 to 3 K.

The RF and optical beams encounter the splitter after reflecting from the secondary mirror, which reflects RF and optical simultaneously. There is no collimation before the RF/optical beam splitter, and thus a cone of rays is incident. However, the beam splitter location on the first beam-waveguide mirror does permit it to be flat rather than curved, which simplifies manufacture. The splitter is tilted at a 45-deg angle relative to the chief ray of the beam. Since a specific light baffle design is lacking at this stage, it is assumed that the splitter will be illuminated by the Sun through the opening beam waveguide for certain antenna tracking positions. The present design calls for four splitters of three different sizes, as depicted in Figure 1. Three different sizes are required to match the light bundles from the symmetrical layout of the primary mirror segments with the asymmetrical fashion in which these light bundles are distributed over the splitter by the diverging beam. Figure 2 depicts the cone of rays incident on the tilted beam splitter.
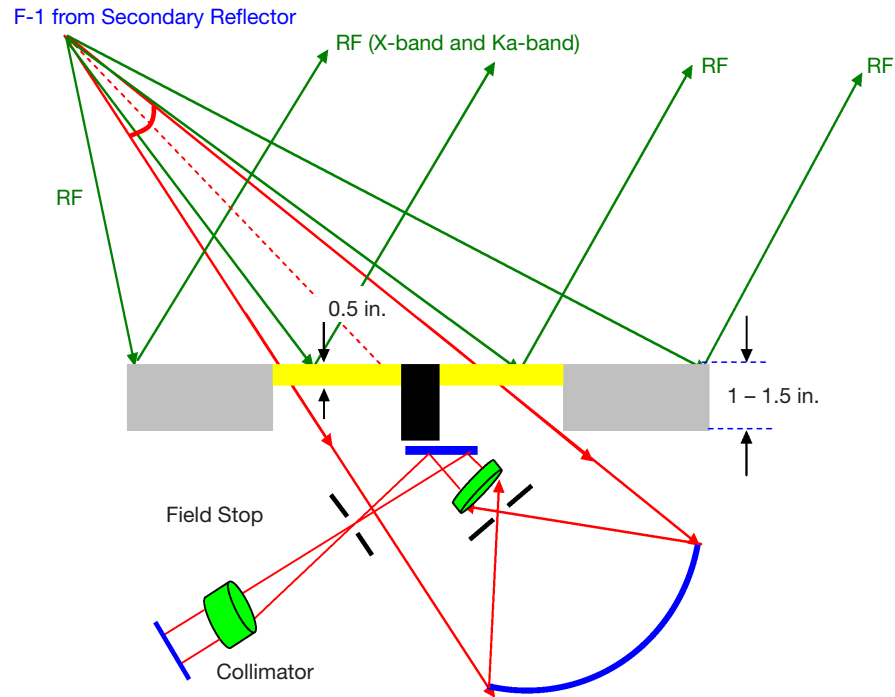
Figure 2. RF/optical beam splitter (side view).

Three options have been identified for accomplishing the RF/optical split:

(1) An interference filter

(2) A gridded metal layer on the glass with a protective coating

(3) Indium tin oxide (ITO) technology

In addition, the existing solar energy rejection filter was examined with respect to its RF/optical beam-splitting potential.

An interference filter consists of several layers of dielectric materials having different refractive indices with some metallic layers as well. These filters are wavelength-selective, using the interference effect between the boundaries of the thin films. Interference filters often require several layers for optimization of the transmission for a particular frequency, bandwidth, and angle of incidence. The large difference between the RF and optical wavelengths poses a significant challenge, partly due to the skin depth requirements for an effective RF reflector. In addition, as mentioned above, introduction of dielectric materials into the RF path can easily introduce system noise if even a small amount of noise is present as a result of the filter.

In the gridded metal-on-glass option, a mesh RF antenna is literally built on top of the glass substrate to reflect RF while transmitting 1550 nm. The technology would combine photolithography to develop the mask for the RF antenna and vapor deposition in vacuum

chambers to deposit a protective coating on the glass. The distance between the grid lines must be smaller than half a wavelength at 32 GHz (Ka-band), and the coating thickness has to be at least equal to the skin depth of X-band, in order to reflect both bands. The skin depth at 7.2 to 8.6 GHz (X-band) for aluminum is about 0.8 μm, which is almost double the skin depth of Ka-band since the skin depth is inversely proportional to the square root of the frequency. The challenge for this option is to optimize the size of the glass substrate and the protective coating such that the noise contribution to RF is negligible. The transmission at 1550 nm would be directly proportional to the area not covered by the aluminum grid. A honeycomb pattern of lines with about 4 mm width on each hexagon is proposed for RF–optical separation. Here, we would want the metallic lines on the glass to be as narrow as possible, perhaps as thin as 0.2 mm. Whether this is a viable option would require additional subject to test and evaluation. One significant drawback of this option is the introduction of significant diffraction into the received optical beam.

Transparent conductive coatings are a comparatively new technology for producing the beam splitter. ITO coatings are optically transparent, electrically conductive films with excellent durability, and have high visible and near-infrared transmission. Depending on the sheet resistivity, these coatings can be utilized in numerous applications such as electromagnetic interference/radio frequency interference (EMI/RFI) shielding, static elimination, de-icing, holography, and the present application [2]. They are extensively used in applications where conductive grids and screens, as explained above, introduce unacceptable degradation in the system's performance. Low resistivity ITO films also exhibit good RF reflectance and can be applied to a wide range of substrates. Sheet resistivity can be varied from 7 ohms/m^2 to 200 ohms/m^2 and up depending on the level of RF reflectance. The standard optical transmission efficiency at 1550 nm is about 82 percent without an antireflection (AR) coating. However, up to 86 percent transmission characteristics can be obtained by overlaying the ITO layer with an AR coating, and we anticipate that 90 percent transmission will be achievable after combining AR coatings with further optimization of the ITO layer. This technology has been selected for further experimental validation in this early study.

Two beam splitter evaluation samples with an ITO coating were provided by JDS Uniphase (JDSU) Corporation,[1] and were tested for RF reflection and 1550 nm transmission at JPL. The sample sizes were 2×2 in. and 1×1 in. The tested samples were optimized for normal incidence performance in the visible. Expected optical transmission was approximately 85 percent at 1550 nm. Future tailoring of the coating for 1550 nm performance at a 45-deg angle of issue is expected to be straightforward. The conductance of the samples is ~14 ohms/m^2.

The RF reflectivity of the beam splitter sample was measured using an automated network analyzer and a waveguide test fixture. Scattering parameters were measured directly and converted to determine RF reflectivity of the sample. Results for reflectivity in broad frequency bands encompassing the DSN bands at 8.45 and 32.0 GHz are depicted in Figures 3 and 4. Measured reflectivity in both the DSN communication bands is approximately 90 percent. Use of a waveguide to make the reflection measurements implies that the field
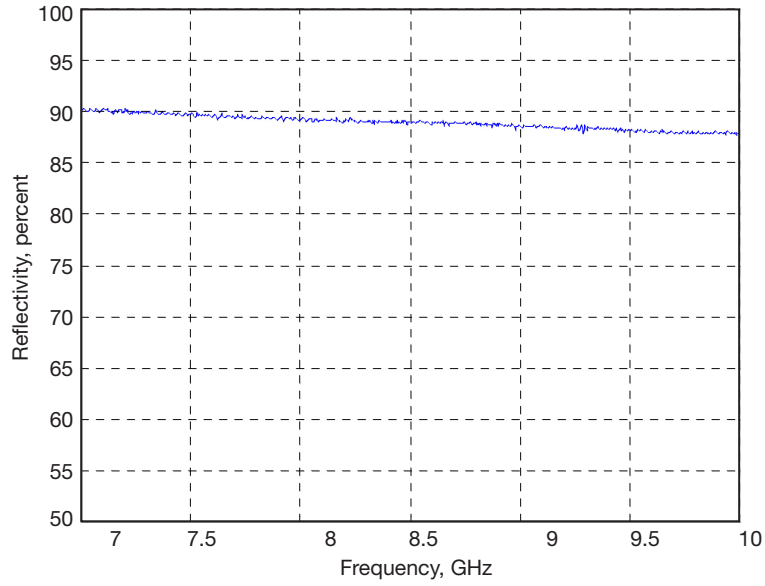
---

[1] http://www.jdsu.com

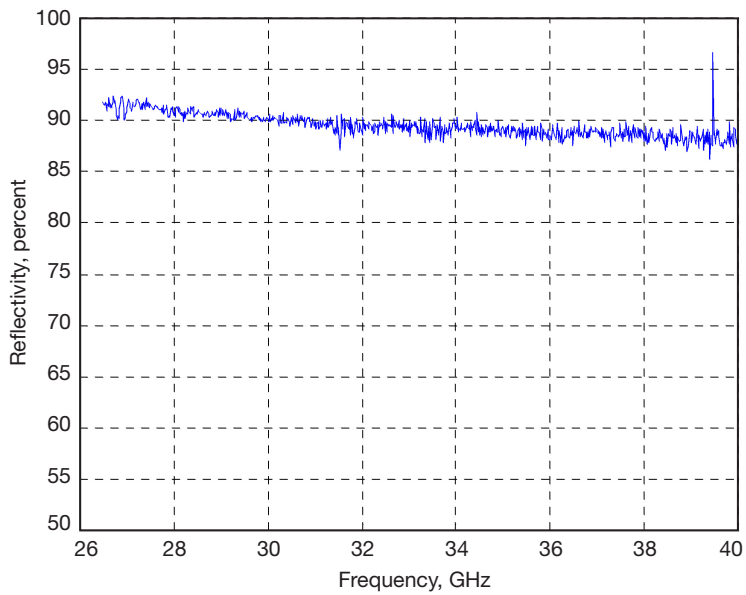**Figure 3. Beam-splitter reflectivity at X-band.**

Figure 4. Beam-splitter reflectivity at Ka-band.

must form a waveguide mode to match the boundary conditions on the walls. This mode can be decomposed into two plane waves glancing off the side walls as the mode travels down the guide. These plane waves are propagating at an angle with respect to the wave-guide axis, with an angle that depends on the waveguide dimensions and the wavelength. Far above waveguide cutoff, the field propagates directly along the guide axis (normal incidence on a sample), but near cutoff, it propagates at a large angle with respect to the guide axis (parallel to the sample in the limit). Thus, waveguide measurements of reflection versus frequency are also measurements of reflection versus incidence angle. In a WR-28

waveguide, 45 deg incidence corresponds to 30 GHz, and about 90 percent reflection. In a WR-137 waveguide, 45 deg corresponds to 6 GHz, which falls off the measured data, but linearly interpolating gives about 91 percent reflection. In fact, the splitter reflection tends to rise slightly for lower frequencies in both bands, even though the coating is becoming thinner with respect to the wavelength. It is likely that the rise is actually caused by the change in incidence angle. Lower frequencies imply a larger angle of incidence, which is consistent with better reflectivity. These measurements indicate that a thicker/better coating would be required for increased RF reflectivity. However, the increase in thickness may adversely impact the transmission of the splitter at 1550 nm. This will be the subject of future experiments.

Transmission measurements on the sample at 1550 nm for normal and 45-deg incidence were carried out. In the test setups depicted in Figure 5, the laser source is just outside the upper left of each image, and the beam passes through the orange circular pellicle beam splitter and to the test optic near the center left of each image. The power is measured by the InGaAs power meter head that has a blue cable leading to it and appears near the center of each image.
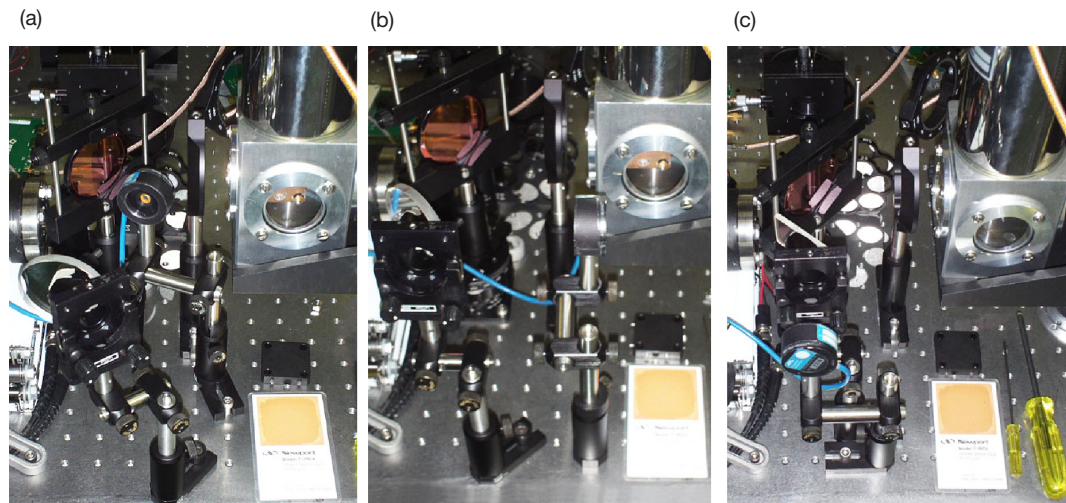

Figure 5. Optical measurement configuration: (a) Testing of sample mirror reflection at about 14 deg incident angle; (b) testing of sample mirror reflection at about 45 deg incident angle; (c) testing of the sample RF/optical separator transmission at 45 deg incident angle.

The measured data are summarized, along with a number of other sample measurements, in Table 1. Splitter data are given in the last two rows of the table. Optical transmission values near 85 percent were measured for normal incidence and 82 percent for 45 deg incidence. This lower value of transmission was expected since the ITO samples did not include an AR coating. It is expected that the AR coating will improve the laser transmission to 90 percent while still preserving the RF reflection at 90 percent or better.

In conclusion, these preliminary beam-splitter results are quite encouraging, and indicate that an acceptable final design with greater than 90 percent, and perhaps 95 percent RF re-

Table 1. Optical efficiency of sample mirrors and RF/optical separators (red numbers).

Tested Optic/ Identifier	Source Ref. Value*	Reflection at 14 deg**	Source Ref. Value*	Reflection at 45 deg**	Source Ref. Value*	Transmission at 0 deg**	Source Ref. Value*	Transmission at 45 deg**	Comments
Round Mirror/ Red Dot	551.4/ 0.07	526.3/ 0.954	551.4/ 0.07	529.1/ 0.960	535.8/ 0.000	0.000 nW/ 0.000 nW	535.8/ 0.000	0.000 nW/ 0.000	Good Reflection Efficiency
Round Mirror/ Unmarked	551.4/ 0.07	526.8/ 0.955	549.4/ 0.07	526.2/ 0.957	535.8/ 0.000	0.000 nW/ 0.000	535.0/ 0.000	0.000 nW/ 0.000	Good Reflection Efficiency
Rectangular 1064 Mirror/ Unmarked	551.4/ 0.034	78.58/ 0.142	551.4/ 0.034	28.45/ 0.052	535.8/ 0.000	479.6 µW/ 0.895	535.8/ 0.000	465.3/ 0.868	Unaccept. Reflection Efficiency
Rectangular 1064 Mirror/ Marked 2#	551.4/ 0.037	79.15/ 0.144	551.4/ 0.037	53.21/ 0.096	536.0/ 0.000	481.6/ 0.898	536.0/ 0.000	457.3/ 0.853	Unaccept. Reflection Efficiency
RF Separator/ Large	551.4/ 0.044	20.15/ 0.037	551.4/ 0.053	81.55/ 0.147	541.4/ 0.000	453.9/ 0.838	541.4/ 0.000	439.7/ 0.812	Fair Transmis. Efficiency
RF Separator/ Small	551.4/ 0.053	19.48/ 0.035	551.4/ 0.046	31.10/ 0.056	541.6/ 0.000	463.5/ 0.856	541.6/ 0.000	446.2/ 0.824	Fair Transmis. Efficiency

* µW/background
** Measured value, µW/decimal efficiency

flectivity and at least 85 percent 1550 nm transmission, is quite feasible. Additional samples have been ordered and will be tested to further quantify the trade-off between RF and optical performance of the splitter.

In addition, JDSU Corporation also performed preliminary calculations that consider astigmatism introduced into the diverging optical beam by the beam splitter, substantial compensation of such astigmatism by the deliberate introduction of a wedge in the splitter substrate, overall tolerance, sag, and mechanical mount effects. Preliminary results indicate that all of the required specifications for the beam splitter in these areas can also be met.

For completeness, an optical solar rejection filter consisting of a multilayer spectral coating on a flexible membrane that had been designed to be placed in front of the 200-in. (5.08-m) Hale telescope on Mt. Palomar [3] was also characterized in the DSN RF bands. The filter is intended to protect the telescope against solar radiant flux and limit solar heating of the interior of the telescope dome while transmitting light at the 1064-nm wavelength of the Mars Laser Communications Demonstration [4]. This filter may also prove useful in the combiner RF/optical ground station. Thus, the RF reflection/transmission properties of this filter are also of interest, even though it was not designed with RF performance in mind. Reflectivity in the Ka-band was measured at approximately 75 percent and is expected to be significantly lower at X-band. We conclude that the solar filter alone cannot be used to separate the RF and optical signals with suitable efficiency. It is possible that further work on the filter could improve the efficiency since RF performance was not considered in the

original design. However, given the success of the ITO splitter described above, further work on the solar filter does not seem warranted for the shared-aperture concept in the present project.

V. Operation of the Optical Terminal in an Open-Air Environment

Despite the difficulties of tracking in the wind and dealing with weather conditions, current DSN antennas do not include radomes. Quite simply, this is because even state-of-the art radomes have RF losses on the order of 1 dB, or 25 percent. In addition to the loss in effective collection area, the 300-K radome loss would cause an increase in system temperature of at least 50 K. The overall effect of the radome would be to reduce the performance of the 34-m antenna aperture to that of a 20-m aperture or less. This is an unacceptable trade, and thus we must assume that no radome will be present for the combined RF/optical ground station.

Optical communication has often been proposed in association with the use of a relatively conventional telescope enclosed in a radome, or more specifically, a shuttered telescope dome. The radome has been an important element in the system due to its ability to block wind, protect the optics from the weather, and reduce stray light from direct sunlight falling on the optics at an oblique angle. The latter is important because the optical line of sight to the deep-space terminal is often available only during the day. A 2001 study [5] concluded that the dome should have wind screens in its shutter opening, plus a solar energy rejection filter to cover the area directly in front of the optical terminal telescope. This combination reduces the effects of solar heating and wind, and better protects the optics from dust.

In the case of a combined optical terminal and RF antenna, the considerable mass of the antenna, and the associated longer period natural resonant frequency, help mitigate the effect of wind gusts. However, maintaining adequate image stability during acquisition may be a challenge. To provide an adequately stable image for acquisition, one solution would be to coordinate the use of an inertial measurement unit (IMU) with a fine-steering mirror (FSM) in the optical receiver assembly. The FSM permits rapid correction of angular deflections up to a few hundred μrad. This is discussed further below.

Cleanliness of the optics is very important in an "outdoor" optical system. Durable optical surfaces to withstand frequent cleaning are helpful in this area. These two items are discussed below. Stray light and solar heating issues are to be addressed in future efforts. The Very Energetic Radiation Imaging Telescope Array System (VERITAS) gamma-ray observatory is an example of a facility that operates optical telescopes in an open-air environment.[2] Although the gamma-ray application requires less stringent cleanliness and surface figure requirements than the optical communications scenario, lessons learned on mirror durability and cleaning methods through VERITAS contacts have been very useful for the current study. In the next three sections, we discuss mirror materials, cleanliness, and contamination control.

---

[2] http://veritas.sao.arizona.edu/

A. Mirror Materials

In this section, we discuss considerations for the primary reflector mirror panels associated with the shared-aperture strawman design. In this case, we must consider mirror reflectivity at 1550 nm, surface quality, and durability of the optical materials in an open-air environment. This design calls for an overall detector field of view of no more than 50 μrad. Given the detector field of view (FOV), atmospheric seeing (λ/r_o), stray light allocation, and other factors, the surface figure error is allocated approximately 10 μrad in this application. This requirement is stated in terms of 85 percent encircled energy (e.g., collection efficiency) and dictates the surface slope error (figure) and the acceptable degree of small period (though not microscopic) surface ripple. The bidirectional reflectance distribution function (BRDF) allocation for microscopic surface roughness, e.g., 10^{-2}, drives the surface finish.

Unlike a typical indoor telescope, the "outdoor" nature of the combined RF antenna and optical terminal requires more robust surfaces that will withstand the weather and endure relatively frequent (perhaps even daily or weekly) cleaning.

Several approaches were initially considered, including means to protect conventional optics from the elements. These approaches included a transparent radome, a substrate located only in front of the optical mirrors, replaceable substrates that are contacted to the optical surface, and substrates having an electrostatic charge intended to repel dust. All of these approaches result in additional optical loss. Additional surfaces also provided more possible system failure modes. A discussion of one active cleaning concept is provided below.

Metallic mirror coatings used for various applications include aluminum, gold, rhodium, and silver, to name a few. Here we discuss some options for fabrication and coating of the mirror segments that produce an efficient RF and optical reflector.

If large optical figure errors are allowed, as in the all-metal strawman design, an obvious choice for the primary mirror segments would be the RF antenna aluminum panels. Aluminum is widely used as a coating material due to its high reflectivity. Anodization reduces the reflectivity by only a few percent, but substantially improves the material's ability to sustain desert-type environmental effects. An anodized coating is grown on aluminum by passing an electrical current through an acid electrolyte bath in which the aluminum is immersed. Some inexpensive techniques of testing and cleaning the anodized aluminum coating have already been established and published for VERITAS and other gamma-ray telescopes. Additional study is required to quantify the ultimate surface roughness achievable, associated cost, and durability of the panels proposed in the all-metal strawman design. If acceptable panel performance can be achieved in a cost-effective manner, the noninvasive nature of the design and low-mass feature would make it a game-changing concept for the combined terminal. Future study in this area is planned.

An aluminum coating on an optical-quality substrate is capable of providing adequate optical performance, since the optical substrate functions to support the aluminum coating. This aluminum can then be overcoated with a durable coating such as TiO_2/SiO_2. The approach ultimately proposed in this phase of the present study is the use of "durable"

optics. A good example of durable optics includes the exterior rear-view mirrors that have been used on automobiles over the last several years. Some of these mirrors last for years, even when no special precautions are taken in cleaning them. Modern automotive exterior rear-view mirrors use a TiO_2 coating over an SiO_2 coating. Therefore, this was one of the first options we explored for durable optics. When these coatings are applied over a metallic coating that is thick enough to provide the required RF skin depth but thin enough to minimize excessive deformation from pressure on the surface, the combination is a relatively durable coating that efficiently reflects both RF and the optical wavelengths of interest.

The preliminary requirements for the primary segments required in the shared-aperture strawman design are given below:

- Substrate: glass (borosilicate)

- Dimensions: 600 mm hex point to point (± 3 mm)

- Edge thickness: 55 mm (nominal)

- Back surface: ground flat

- Surface profile: spherical

- Focal length: 12.2 m (±3 mm)

- Spot size: 10 μrad (measured at radius of curvature); >85 percent of Airy pattern

- Surface peak to valley: <1000 nm

- Peak to peak RMS: <500 nm

- Microripples on surface: <60 nm with period of 3 cm

- Microscopic surface roughness: <20 nm

- Bevels: 1 mm (nominal) at 45 deg

- Coating: aluminum with protective overcoat

- Coating type: aluminum on top of the glass substrate + TiO_2+SiO_2

- Average reflectance angle from the rays off the secondary: 14 to 17 deg

- The aluminum must thick enough to reflect the RF at X-band and Ka-band

Display Optics [6], the vendor that fabricated the VERITAS mirror segments, was contacted, and several sample mirrors were ordered for preliminary analysis and testing at JPL. A compromise between requirements and cost relaxed the requirements slightly, with a final specification of 405 mm segment size, ±25 mm focal point uncertainty, and 20 μrad for the spot size. More than an order of magnitude reduction in cost was achieved by relaxing the requirements in order to mitigate the risks through preliminary BRDF and environmental damage test before requirements are finalized for the real mirrors. Testing and characterization of these samples will appear in a follow-up article.

We have also obtained some small mirror samples from a second vendor, China Optical Coating Laboratory, Inc.,[3] and here we report tests on those samples. The size of these small

---

[3] http://www.chinaocli.com/index1.htm

samples is 60×6.5 mm. The thickness of the aluminum layer is 20 μm, while the thickness of TiO$_2$/SiO$_2$ coating is 10 μm. The substrate was glass (K9) with a flatness of 1 μm. Since the skin depths for RF reflection at Ka-band and X-band are approximately 0.4 μm and 0.8 μm, respectively, this thickness of aluminum is much more than adequate for our application. The reflectivity of these small sample mirrors was measured at 1550 nm in both DSN bands. Measured reflectivity at 1550 nm was greater than 95 percent and is summarized in the first two rows of Table 1. Measured reflectivity in the two DSN bands was also excellent, exceeding 95 percent, and these results are summarized in Figures 6 and 7. At this time, the durability of the coating has not been assessed in any quantitative way, but is expected to be satisfactory. This will be the subject of future testing.

B. Cleanliness

One of the main concerns associated with operation of the ground station in an open-air environment is mirror cleanliness. Particle accumulation on the mirror has two detrimental effects: (1) a decrease in mirror reflectivity, and (2) an increase in the mirror's susceptibility to scattered light. The latter effect is greatly magnified when a mirror (or a telescope) is at a small angular distance from the Sun that in operational conditions corresponds to a small Sun–Earth–probe (SEP) angle.

The BRDF[4] is a measure of this susceptibility. Here we give a brief description of BRDF, and how it relates to the optical communications system.

In general, there are two major mechanisms for background radiation to enter the communications detector. The first is through direct illumination of the detector from the diffuse sky background light, P_{bg}. In this case,

$$P_{bg} = L_\lambda FOV_{sr}\Delta\lambda(\pi/4)D^2\eta_{rx}$$

where L_λ is the sky radiance (W/sr/nm/m^2), FOV is the detector field of view (sr), λ is the filter bandwidth, D is the telescope aperture, and η_{rx} is receiver efficiency.

In the presence of contamination (e.g., dust) or mirror roughness, the Sun-related stray light radiation reaching the detector can be computed if the BRDF of the (primary) mirror is given:

$$P_{sl} = \{I_\lambda BRDF(SEP)T(\lambda)\}FOV_{sr}\Delta\lambda(\pi/4)D^2\eta_{rx}$$

where I_λ is the Sun irradiance (W/ nm/m^2), FOV is the detector field of view (sr), λ is the filter bandwidth, D is the telescope aperture, η_{rx} is receiver efficiency, T is the atmospheric transmittance, $BRDF$ is measured in units 1/sr, and SEP is the Sun–Earth–probe angle. From this equation, we see that as far as the total background light is concerned, the following equivalence can be identified:

$$L_\lambda \Leftrightarrow \{I_\lambda BRDF(SEP)T(\lambda)\}$$

---

[4] J. E. Harvey, "Light-Scattering Characteristics of Optical Surfaces," Ph.D. dissertation, University of Arizona, 1976.
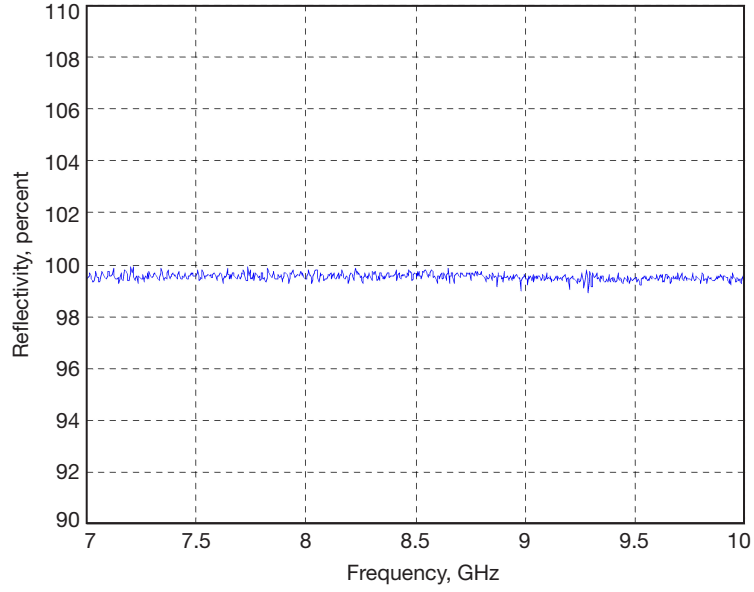
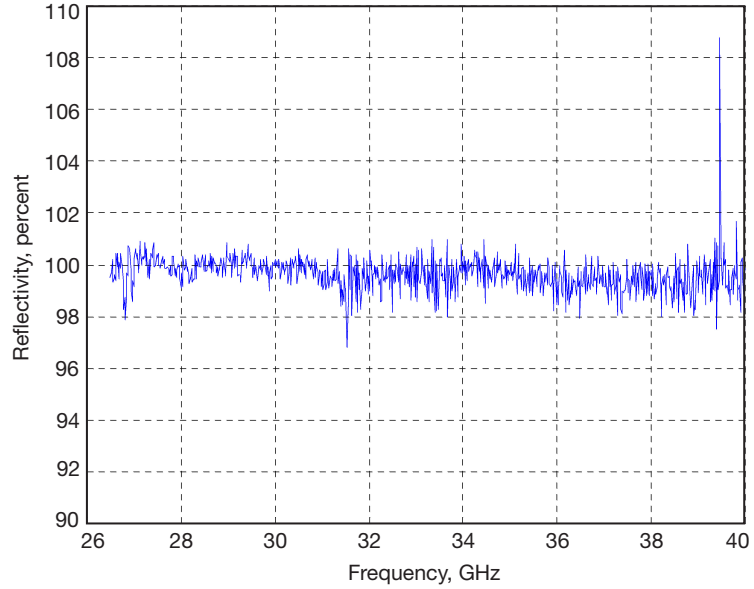**Figure 6. Mirror reflectivity at X-band.**

Figure 7. Mirror reflection at Ka-band.

Thus, a nonzero BRDF indicates that specular sunlight from the SEP angle will be scattered from the surface in a diffuse manner and become indistinguishable from the diffuse background. The BRDF is a generally a decreasing function of the SEP angle, and rises rapidly for small angles. Thus, the closer the Sun is to the probe, the smaller the SEP angle, and the larger the portion of the specular sunlight that is scattered onto the detector. For example, if we approximate the transmission as unity, then when

$$BRDF(SEP) = L_\lambda / I_\lambda$$

the amount of background due to scattered sunlight and diffuse background will be equal. As an example, consider the case of SEP = 3 deg and elevation angle of the telescope of 20 deg. Using the MODTRAN radiative transfer software program to understand the possible sky radiance at the Goldstone Deep Space Communications Complex (modeling the desert aerosol distribution with a wind speed of 6 m/s), one can obtain that the sky radiance at 1550 nm is L_λ = 2E–3 W/cm^2/sr/μm; knowing that I_λ = 0.0269 W/cm^2/μm, we find that for a BRDF = 0.0743/sr, the background noise generated by the stray light will be the same strength of that generated by sky radiance.

An approximate model for the BRDF of a contaminated mirror is the Harvey modified model [7]:

$$BRDF(SEP) \approx \left\{ b_o \left(100 | SEP | \right)^{S_o} + b_1 \left(1 + \frac{| SEP |^2}{l_1^2} \right)^{S_1/2} + b_2 \left(1 + \frac{| SEP |^2}{l_2^2} \right)^{S_2/2} \right\}$$

Here, the coefficient b_o is related to the microroughness of the mirror and is wavelength dependent. The coefficients b_1 and b_2 depend on the dust coverage of the mirror and are dependent on the wavelength as well. The coefficients l_1 and l_2 control the knee of the scattering curves. In practice, the Harvey coefficients are derived by measurements of scattered light at different dust concentration levels.

In the present application, we intend to specify the mirror roughness and thus b_o will be controlled. The other coefficients will evolve in time as the mirror contamination increases. The rate of particle contamination will ultimately determine how often mirror cleaning is necessary. The frequency of cleaning will then determine the longevity of the mirror surface. In addition to the BRDF, we are also interested in the evolution of the mirror reflectivity with time.

In order to evaluate the contamination environment at Goldstone, five small sample mirrors were placed on the DSS-13 antenna at various locations and the BRDF and reflectivity were measured using a hand-held meter[5] on a daily basis. Figure 8 depicts the location of the five test mirrors. Mirrors 1 to 3 were placed face-up at 120-deg intervals on the primary reflector at a radius of approximately 5 m from the center of the primary. Mirror 4 was placed face-down on the underside of one of the steel members making up the quadripod support structure. This mirror is intended to simulate contamination that would occur on the secondary. A fifth mirror was placed on the quadripod at a right angle with respect to the previous four.

Figures 9 and 10 depict the mirror BRDF at an SEP of 25 deg, as measured by the BRDF meter, as well as the instrument's estimate of mirror reflectivity. As expected, we see a gradual degradation in mirror performance with time. We note that mirror 4, which is placed upside-down on the structure, is relatively unaffected in terms of BRDF, presumably since particles do not settle on the mirror as readily. This mirror's measured reflectivity was highly variable and is omitted from the plot in Figure 10. From Figure 9, we see the extreme
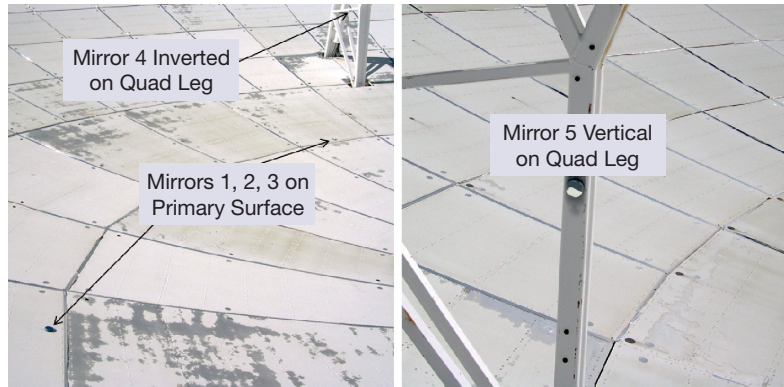
---

[5] http://www.schmitt-ind.com/products-services-measurement-systems-microscan.shtml

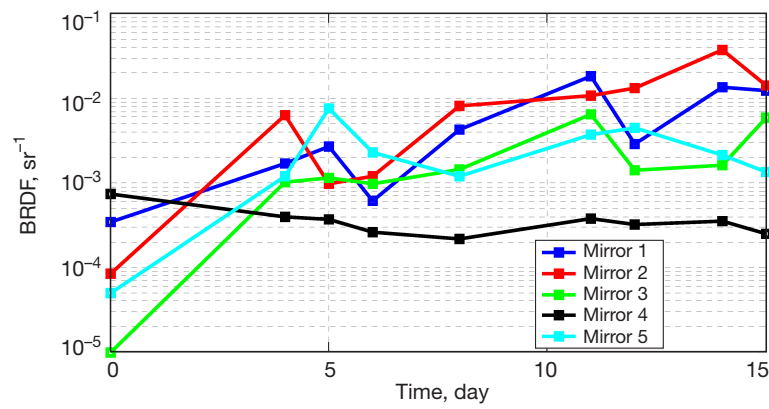**Figure 8. Mirror locations for contamination testing.**

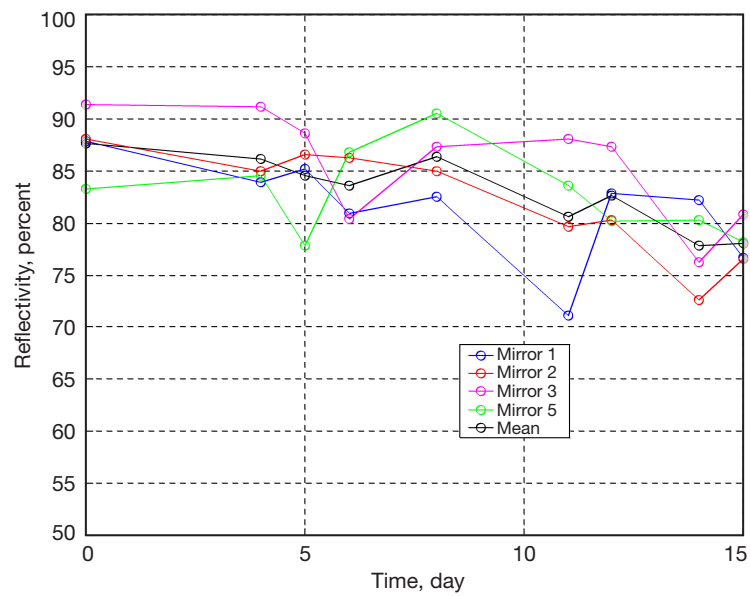**Figure 9. Measured BRDF versus time on the sample mirrors.**

Figure 10. Mirror reflectivity versus time.

sensitivity of the BRDF to contamination, an increase of three orders of magnitude in only 15 days of exposure. The reflectance degrades from approximately 88 percent to 78 percent over the same elapsed time.

The next step in the contamination analysis is to remove the effect of the BRDF due to surface roughness from the measurement and fit the change in BRDF over time by the BRDF evolution we would expect from a constant contamination rate measured in units of percent of surface/hr. The results of this fit are illustrated in Figure 11. This very approximate fit, using the limited data set available, results in a particle accumulation rate of 0.033 percent/hr. This value is quite consistent with expectations [8]. For example, an accumulation rate of 0.04 percent /hr has been measured for Apache Point,[6] an environment similar to Goldstone.
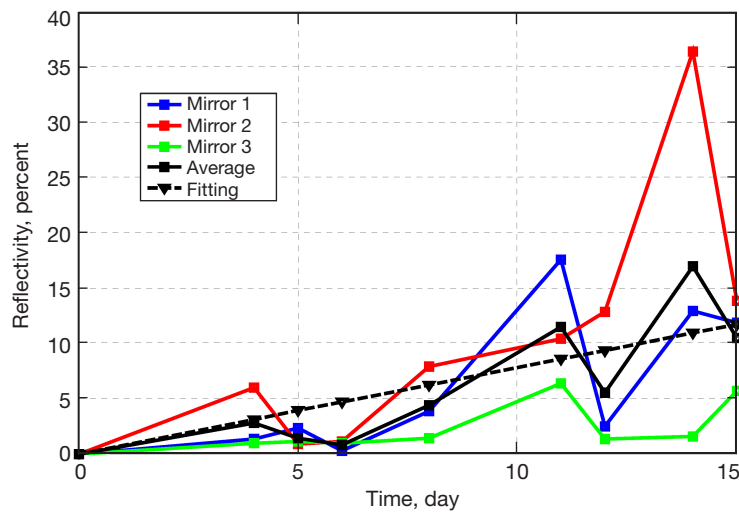

Figure 11. Change in BRDF on the mirrors versus time along with a linear fit.

We plan to pursue additional contamination measurements in the future, but for now we may use the contamination rate to estimate the frequency of mirror cleaning required for a given scenario. Dust coverage and mirror microroughness contribute independently to the additional induced radiance/noise on the detector. Figure 12 shows the radiance due to dust contamination and Figure 13 shows the radiance due to surface roughness, both for an SEP angle of 3 deg and 1550 nm. For reference, the nominal diffuse background radiance is approximately 2E–3 $W/cm^2/str/\mu m$. These figures indicate that if we arbitrarily limit the scattered light from contamination to be no greater than the diffuse background, we must maintain a cleanliness level of approximately 600. Likewise we would also require a mirror microroughness of better than 12 nm. Additionally if, for example, we have chosen an excellent surface roughness specification of 2 nm, it would be prudent to maintain the cleanliness of that surface at around 150 in order to keep the scattered light contribution equally low. A poorer mirror with 20 nm roughness corresponds to a cleanliness level of only 750.

Figure 14 illustrates the conversion from cleanliness level to percent dust coverage on the surface. Using this plot and a conservative contamination rate at Goldstone of approxi-

---

[6] R. Hubbard, "Stray Light," presentation at Advanced Technology Solar Telescope (ATST) Conceptual Design Review, September 2002.
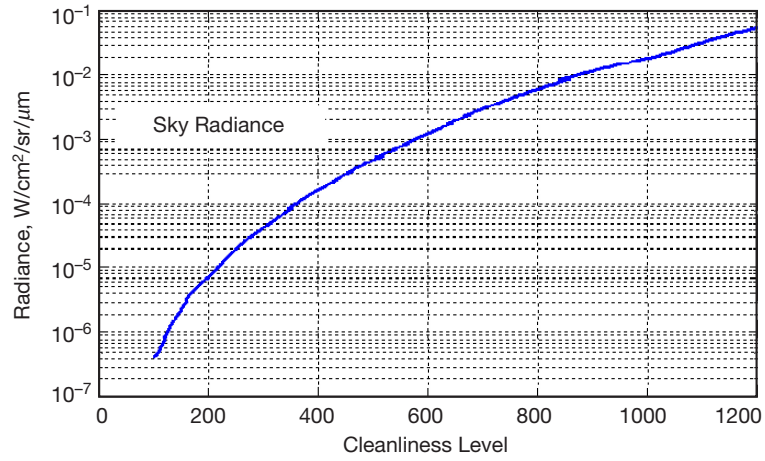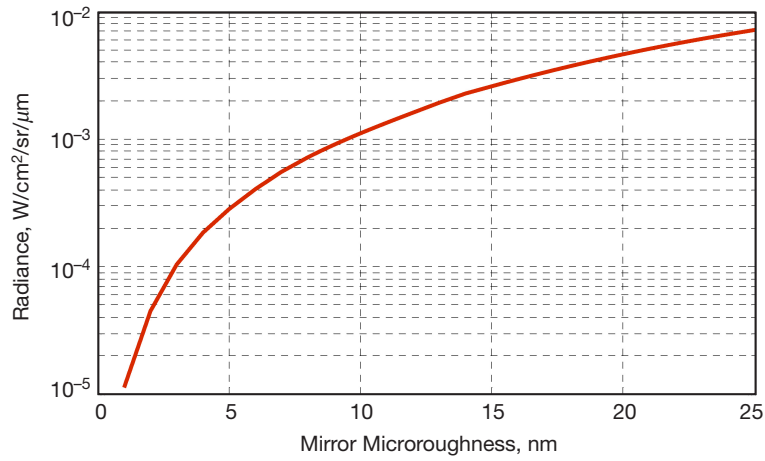
Figure 12. Radiance versus cleanliness level.

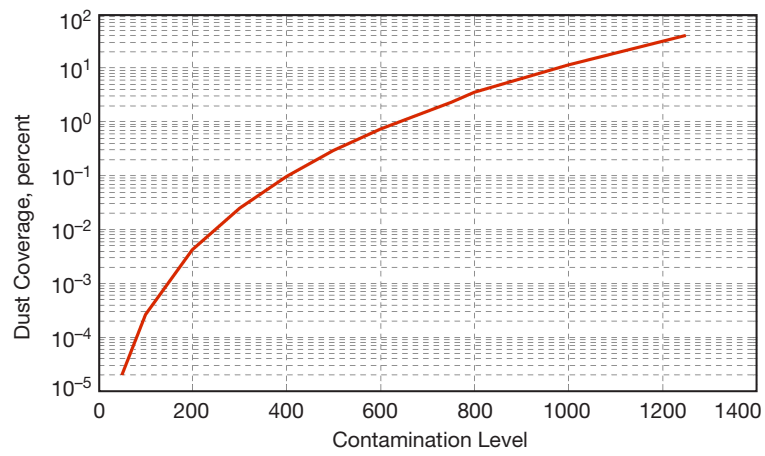
Figure 13. Radiance versus microroughness.

Figure 14. Contamination level versus dust coverage.

18

mately 0.04 percent/hr, we may convert a given contamination rate to a required cleaning interval. Performing these conversions, we find that a cleanliness level of 150 is completely impractical in the Goldstone environment — hourly cleaning corresponds to a cleanliness level of 300, daily cleaning to a level of 600, weekly cleaning to a level of 750, and biweekly cleaning to an unacceptable level of 1100. Thus, for near-Sun tracking we may expect to clean the mirrors nearly daily, and at an absolute minimum, weekly. For the Mars scenario, small SEP angles occur about 70 days every two years, implying 35 mirror cleaning cycles per year to accommodate these small SEP days. These cleaning cycles would be needed in addition to the normal cleaning cycles required to maintain high reflectivity. In practice, for a given mission, near-Sun tracks are not required at all times of the year and the cleaning rate will likely be adjusted based on the upcoming tracking schedule.

C. Active Contamination Control

As the previous discussion indicates, a major challenge caused by lack of a protective dome around the antenna/telescope assembly is dust contamination on the exposed optical surfaces, particularly the primary mirror. As suggested, periodic cleaning is a possible solution, at the expense of increased operations costs and mirror degradation.

An alternative solution is to put an optical window over the entire 10-m-diameter mirror or equivalent aperture. Past experiments and analysis have shown that a glass window for this purpose is not a workable solution due to (1) excessive mass arising from specific thickness requirements (10:1 to 20:1 ratio of diameter to thickness — even for a segmented window); and (2) optical aberrations introduced by the thickness of the glass. To solve both problems, a thin (~5 μm thick) membrane that can be formed in multimeter diameters was identified for an earlier application (multimeter diameter filter at the entrance aperture of a telescope). This technology (for coated or uncoated membranes) is now well at hand. Figure 15 shows a 1.5-m-diameter narrow-band membrane filter developed for JPL's Optical Communications Group (Communication Architectures and Research Section). The membrane material does not degrade with exposure to sunlight, but has integrity limits for wind exposure.

For control of the contamination issue indicated above, a bare (uncoated) thin membrane substrate mosaic protecting the mirror matrix from rim-to-rim is proposed: see Figure 16. This could be a quadrant or a mosaic of multiple segments to form the required 10-m-diameter. Equipping the membrane with optically transparent electrodes (ITO or carbon nanotube) deposited around the edges will allow dust to be swept away to the side electrostatically [9]. This technique has been proven to work effectively for automatic dust removal. AR coating of the membrane will mitigate approximately 8 percent loss introduced by the uncoated membrane, but will cost more. The effect of the membrane on RF performance is likely to be small due to its relatively thin nature, but would ultimately depend on the loss of the material involved. Of more concern is the effect of water accumulation on the membrane during inclement weather. Water on radome surfaces is a significant source of noise temperature [10], and this effect would need to be mitigated in designs where the optical surface is shared by the RF beam as well. For designs where the RF and optical apertures are not shared, the method of contamination control described here would appear to be a vi-

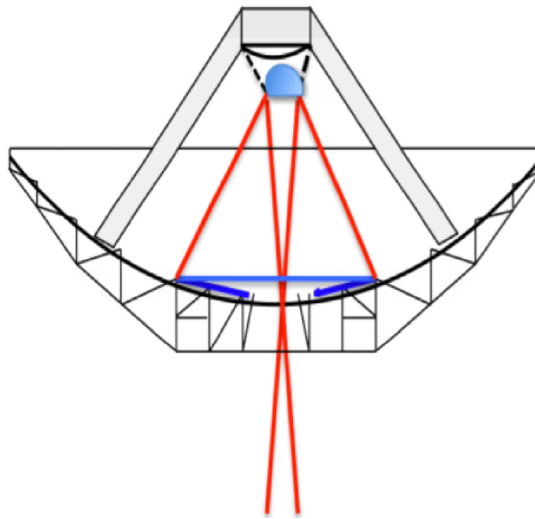**Figure 15. Large-diameter membrane.**

Figure 16. Protective membrane on a 10-m mirror.

able approach, but additional work and prototyping will be required prior to committing to an operational solution.

VI. Acquisition and Tracking

Another key challenge in integrating the RF and optical ground stations is acquiring and tracking both the microwave and optical signals with the shared aperture. The full beam-width of the 34-m aperture at Ka-band is approximately 16 mdeg, or 280 μrad. The field of view for the optical detector can be as small as 50 μrad, or 3 mdeg. Thus, we do not expect the nominal RF antenna pointing performance to be sufficient for the optical system. In addition, the refraction properties of the atmosphere differ at microwave and optical wave-lengths. The local antenna surface distortion due to mechanical effects must also be taken into account. Solar heating and wind will also contribute to local surface distortion. The optical communication system must either provide its own fine-steering system to mitigate

these effects, or accommodate them within the field of view of the communication detector. Here we attempt to bound these factors so that a strawman steering mirror system may be designed. Temporal scales for the effects considered here would determine the bandwidth requirements for the steering mirror system.

A. Nominal Pointing Accuracy

Table 2 summarizes the error sources in the blind-pointing system of a nominal 34-m DSN antenna. The final mean blind-pointing error is in the 2.3 to 8.4 mdeg range. This value climbs to 6.5 to 12.4 mdeg in a 30-mph wind. These values represent the nominal error at acquisition, and hence determine the required pull-in range of any closed-loop tracking system. In the RF bands, closed-loop conical scanning and monopulse tracking [11] can reduce the operational tracking error to a few mdeg. These nominal tracking errors must be accommodated by the optical fine-steering system or detector field of view.

Table 2. Nominal pointing specifications for DSN 34-m antennas.

Error Source	Estimated Size, mdeg	Correction Method	Residual Error, mdeg
Atmospheric refractivity	83 at EL = 10 deg	Surface weather model	0.8, 1σ at EL = 10 deg
Gravity deformation of dish and quadripod	100, EL (max)	Subreflector lookup table	5–10 P-P ($\cong 6\sigma$)
Systematic errors	100, EL (max)	12 term, first-order trigonometric model	1–8 (range)
Azimuth track level	8 P-P ($\cong 6\sigma$)	Lookup table	0.3 XEL, 0.1 EL
Azimuth encoder gear noise	0.44, 1σ	Uncorrected	0.44, 1σ
Elevation encoder	0.2	Uncorrected	0.2, 1σ
Thermal deformation	8 P-P ($\cong 6\sigma$, EL & XEL)	Uncorrected	8 P-P ($\cong 6\sigma$)
Wind displacement of foundation	1.1 (30 mph wind)	Uncorrected	1.1 (3 mph wind)
Wind distortion of structure	6–9 (30 mph wind)	Uncorrected	6–9 (30 mph wind)
Calibration measurements	1, 1σ	Uncorrected	1, 1σ
Mean pointing error (without wind)			2.3–8.4 (range)
Mean pointing error (with 30 mph wind)			6.5–12.4 (range)

B. Atmospheric Refraction

Atmospheric refraction is also an important factor during acquisition and tracking. Currently, the local temperature and humidity are measured and used as inputs to the antenna-pointing model to correct for the bending of the RF beam as it passes through the atmosphere [12]. The dielectric constant of water vapor is higher at RF frequencies than at optical frequencies and optical refraction is relatively independent of humidity [13]. Thus, the difference in pointing correction due to refraction is different in the RF and optical and

depends on the local relative humidity and temperature. This difference is only significant at low elevation angles, and must be accommodated during acquisition of the spacecraft signals. The difference in RF and optical refraction was calculated by using the Lanyi model [12] to calculate the RF refraction and the optical refraction was commuted as described in [13] and differencing the two values.

Figure 17 illustrates the difference in the refraction correction at 20 deg elevation versus temperature. Two curves, representing relative humidity of 20 percent and 60 percent, are included. We see at the extreme case of 60 percent humidity and 40 deg C, which is unlikely to be observed in practice, that the difference in refraction correction is approximately 25 mdeg, or 440 μrad. In order to provide a statistical description of the pointing difference, an estimate of the cumulative distribution of weather conditions at Goldstone was made. Statistics for the worse and best case (1 percent and 99 percent) of absolute humidity for the two extreme months of February and August were used, and a Gaussian distribution of the intermediate values was assumed. This distribution was associated with the expected values of low and high temperatures for those months. Finally, an average month was constructed by averaging these two extreme months.

Figure 18 shows the expected difference of RF minus optical refraction for the three months. The data indicate that there is a 99 percent probability that the pointing difference will be less than 12 mdeg, even in the most extreme month of August. If it is unreasonable for the system to accommodate the refraction difference with a fast-steering mirror system or the communication detector, it is also possible to point the RF beam slightly off boresight, toward the preferred optical direction, to accommodate a portion of this pointing difference. In this case, the RF system would incur some additional loss of signal, a design trade-off for the combined RF/optical system. However, the 16-mdeg Ka-band beamwidth implies that some additional pointing compensation for the refraction effect will need to be included in the optical system design.
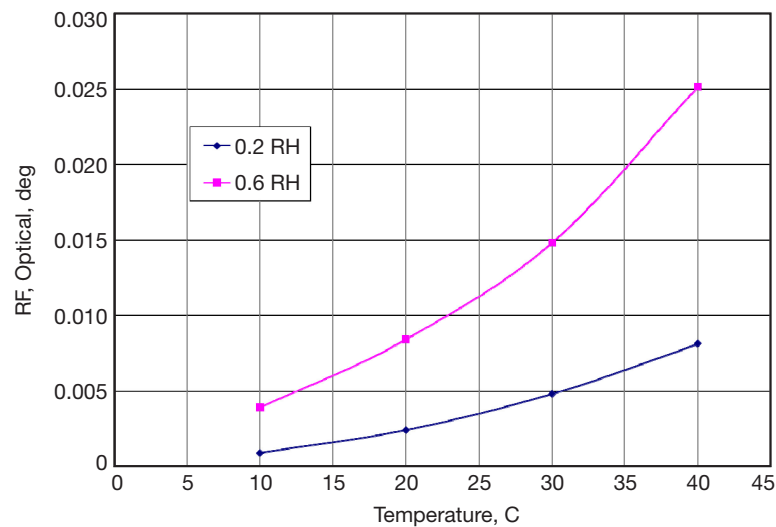

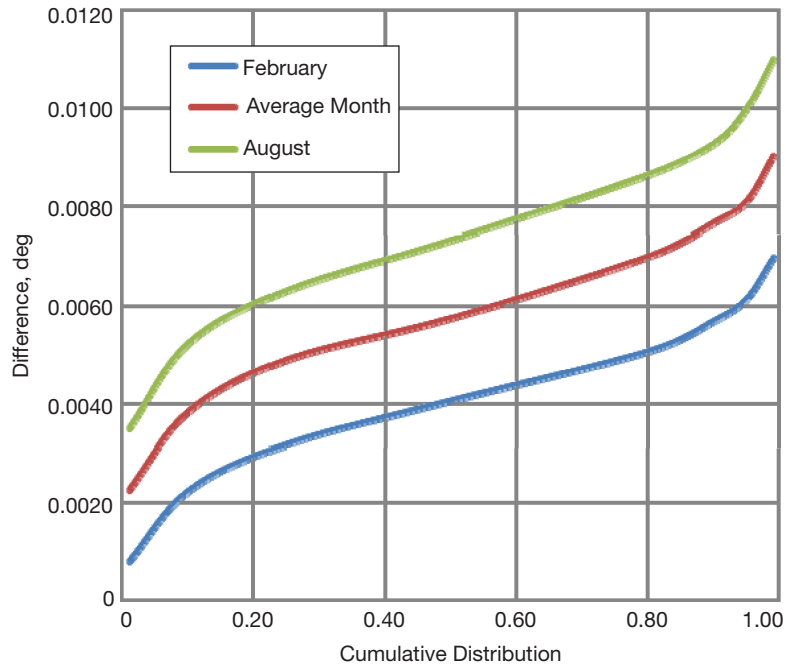Figure 17. Atmospheric refraction effects on the RF and optical beams.

Figure 18. RF and optical refraction difference at Goldstone at 20 deg elevation (901 mb).

C. Antenna Structure and Optical Layout

The structure of a 34-m antenna is larger than that thus far conceived for a stand-alone optical communication terminal. In addition, the RF antenna structure is not designed to maintain the surface figure to the accuracy required for optical operation. Furthermore, the antenna reflector panels are themselves too flexible to maintain an adequate optical figure for a 50-μrad-class detector such as proposed for use with the strawman shared-aperture design. As mentioned earlier, one of the proposed strawman designs proposes to use a much larger detector field of view and accommodate the reflector in accuracies directly.

In the shared-aperture strawman design, the proposed optical receiver surface will be made of optical mirrors, each having enough thickness to maintain the required optical figure. Due to local temperature variations, the proposed mirror panels are each expected to be 60 cm across and about 5 cm thick. Larger mirror panels would be desirable, but information to date indicates that in the absence of long (and expensive) mirror panel annealing times, larger mirror panels would pose more risk of excessive temperature-induced figure error or even breakage from thermal shock in this open-air design. Given that each mirror panel is less than 1 percent of the total optical aperture area, the proposed design organizes the optical mirror panels in groups that are each supported by a substructure that is only connected to the antenna structure at three points. This will help maintain alignment between mirror panels in each group, though it is not yet known if passive alignment of this type will be adequate for the mirrors within each group.

Therefore, the next phase of this study will include analysis to determine if active pointing for each mirror panel will be required. The current assumption is that it is likely that each mirror panel will need to be actuated to some degree. This assumption is based on the fact

that each 60-cm panel can only tolerate about 3 μm of tilt across its width in comparison to neighboring panels in the mirror array in order for the array to maintain adequate optical performance.

Another characteristic of a typical antenna structure is the tendency for the primary reflector dish to "droop" or sag as the antenna is pointed toward lower elevation angles. This is described in further detail below. Building a structure strong enough to reduce this dish surface droop by an adequate degree to adequately maintain even the figure of a continuous optical surface of 10 to 15 m outer diameter would not be feasible, and hence the optical system must accommodate this structural droop.

To address the foregoing issues in the shared-aperture version, the 10-m-equivalent optical area is broken up into four groups of mirror panels, with each group having an area equivalent to a circular 5-m aperture. By using four groups of apertures, it is possible to independently tilt (and piston if necessary) each of the mirror groups in order to compensate for sag in the antenna dish.

It is assumed that the antenna structure, particularly in the region of the optical surface, must be more rigid than that of a conventional antenna, perhaps to an extent that would reduce local structural distortion by a factor of at least two. The cost and design implications of this will be studied in detail in the next phase of this effort. Second, each of the four mirror groups of the optical receiver will require a fine-/fast-steering mirror to provide some independent steering of the receive beam. An FSM for each mirror group is already in the baseline shared-aperture design, but the antenna structural deformation requires that the FSM have more angular range than has been customary. An additional application of the FSM will be to compensate for the difference in atmospheric refraction discussed in the previous section.

An additional consideration for the shared-aperture design relates to the shape and size of the area on the antenna surface utilized for optical. Specifically, it is desirable to limit the outer diameter of the optical area, since this minimizes the structural impact and makes it more practical to use spherical optics for the primary optics.

In this section, we attempt to quantify the distortion of the primary caused by gravity distortion of the backup structure as the antenna tips in elevation. Currently, during an RF track the subreflector's position with respect to the primary is changed as a function of elevation angle. This serves as a first-order correction and recovers some of the antenna gain that would otherwise be lost. In the arrayed telescope design, this motion of the backup structure will directly impact the pointing of the individual telescopes. As described above, in the shared-aperture design, the four subapertures on the primary will experience different local distortions that must be accommodated by their FSM systems. In this section, we bound these effects.

Direct measurements of the antenna surface distortion versus elevation angle have been made using various techniques on several occasions. Figure 19 depicts a large number of corner-cube reflectors that were placed on a 34-m antenna during such a measurement. In
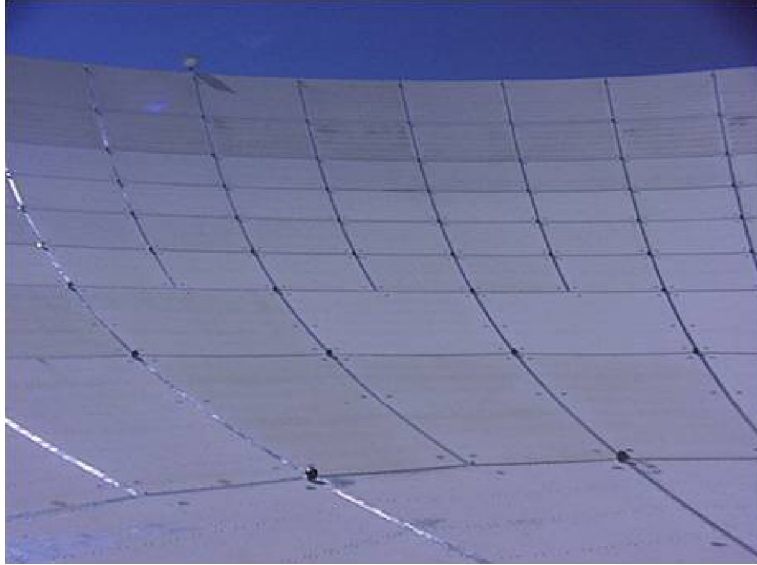
Figure 19. Corner cubes used in the measurement of surface distortion.

this case, the position of each of these cubes was precisely measured using a laser tracker and recorded for a number of antenna elevation angles [14].

Figure 20 shows a map of the measured distortion of the primary reflector at zenith with respect to the surface at the rigging angle for the antenna, 45 deg elevation. Here we see the typical taco-shaped distortion where the surface cups in along the elevation axis and cups out in the perpendicular direction. A relative distortion of opposite sign occurs as the antenna tips below the rigging angle.
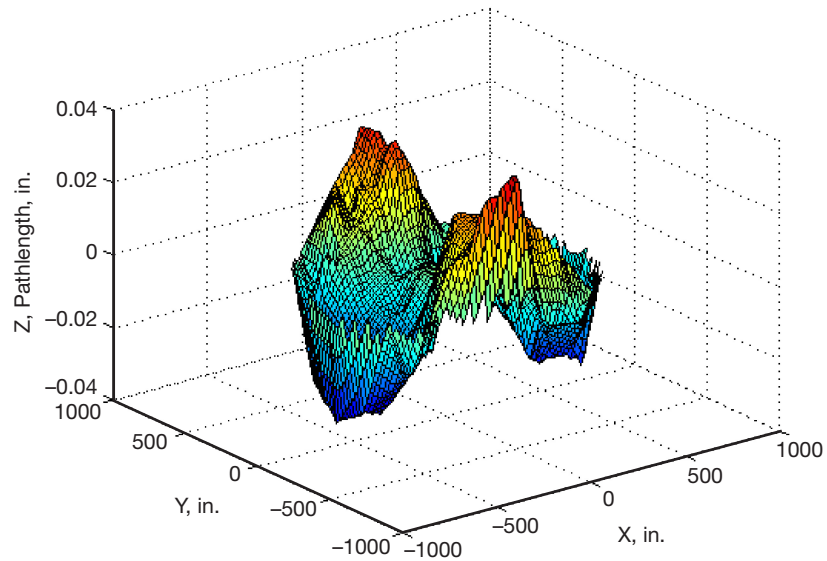

Figure 20. Primary surface distortion, zenith pointing.

For both the shared-aperture and arrayed telescope designs, we are concerned with the local tilt of the primary surface (backup structure) at various locations on the primary. By processing the above data, we may extract the local tilt of the surface. Figure 21 depicts the actual locations of the corner cubes on the surface. We identify 9 rings of data. Here we will report the edge tilt of the various panels as the tracks in elevation. Two different types of panel edges exist, those measured in the ϕ direction, examples of which are shown in the figure as red lines, and edges along the radial direction.
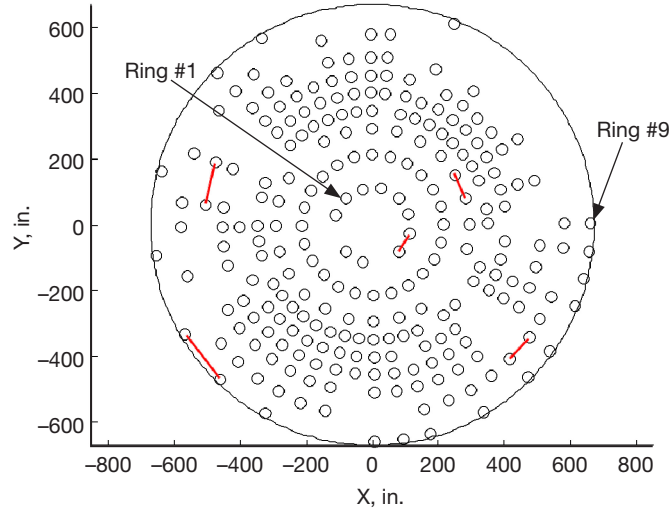

Figure 21. Data points and panel edge definition.

The existing data set was processed and the local tilt angles for the various panels were extracted as a function of position and antenna elevation angle. Typical data, in this case for the ϕ-directed edges of the panels in ring 3, are shown as a function of position and antenna elevation angle in Figure 22. The panel edges are numbered sequentially, and hence the x-coordinate on the plot may also be interpreted as the ϕ location of the panel edge within ring 3. The periodic nature of the taco-shaped distortion is clearly visible as well as the sign change and symmetry of the distortion as the angle changes from 45–15 = 30 deg through 45 deg and up to 45+15 = 60 deg. Similar data are available for all rings as well as the perpendicular panel edges. Somewhat unexpectedly, the peak angles reached by the panel edges are approximately independent of both edge location and edge type. Essentially all edges traverse ±40 mdeg as the antenna tracks through 13 → 90 deg, and ±20 mdeg over an elevation range of 30 → 60 deg. In the case of the shared-aperture systems, the direction of the optical rays reflected for the surface is changed by twice the panel angle. In the case of the arrayed telescopes, the panel angle maps directly into pointing error. In each case, the errors must be accommodated by the optical fine-steering system and/or communication detector field of view.

It is recognized that in the real combined ground station, the surface distortions will differ from those described above. The additional weight of the optics will require significant changes in the backup structure, which will then experience a different gravity distortion than the existing antennas. This is an area that will be examined in the next phase of this
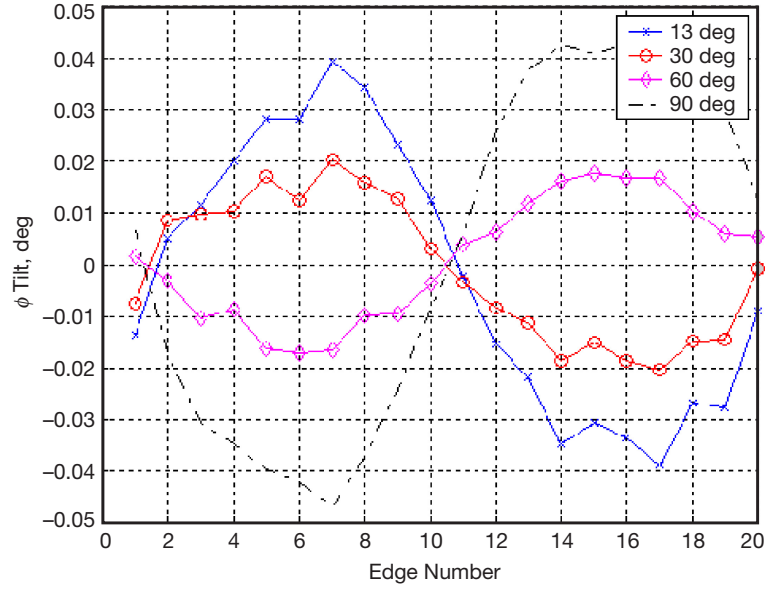
Figure 22. Tilt of panel edges versus antenna elevation angle.

study. Thus, the calculations above serve only to provide initial data on which the strawman design can be based.

D. Structural Changes to the Existing 34-m Antennas

The mass added by the optical aperture is likely the most important factor in determining the structural mechanical requirements for the dual-use system. Approximate mass estimates for the strawman designs as well as a strawman design for the FSM system have been generated. Structural changes to the antenna will be required to accommodate the added weight and maintain a surface deformation consistent with the range of the steering mirror system or detector field of view. This in turn will be a major factor in the cost of the combined system. This work will be carried out in the follow-up phase of the present study.

VII. Atmospheric Turbulence at Goldstone

To correctly study the performance of a ground receiver located at Goldstone, a number of investigations and measurements are necessary to characterize the atmospheric channel at the location itself. An optical channel for optical communications is mainly characterized by the atmospheric transmittance loss, the (daytime) sky radiance, and the clear-air turbulence. To address the atmospheric transmittance loss and sky radiance, a Sun-photometer will be deployed at Goldstone starting November 2009 [15]. After the deployment, some time will be necessary to build consistent statistics. Usually the level of statistical consistency needed in the data are achieved after several years of observation, even if after the first year of data one can have an approximate understanding of the variation of atmospheric transmittance and sky radiance.

Clear-sky turbulence is caused by the random variation of the atmosphere refractive index. For a downlink ground station, one effect of clear-air turbulence is the degradation of telescope resolution caused by the astronomical seeing (S_e), which limits the spot size (d_o) of the focused beam as

$$d_o = S_e F$$

where the astronomical seeing is indicated here in radians, and F is the telescope focal length [16].

The astronomical seeing is generally much larger than the field of view that can be derived by a diffraction-limited telescope (i.e., λ/D, where λ is the wavelength of operation and D is the telescope aperture), and can be expressed as

$$S_e = \lambda r_o$$

where r_o is named atmospheric coherence length and is a measure of the phase distortion experienced by the phase of a (downlink) beam propagating through the atmosphere. The atmospheric coherence length, or Fried parameter, can be calculated using the expression

$$r_o = \left[0.423 k^2 \sec(\theta) \int C_n^2(z)dz \right]^{-3/5} (m)$$

where θ is the angle from zenith, C_n^2 is the refractive index structure coefficient, which is the measure of the turbulence of the atmosphere, k is the wave number, and z is a variable indicating the altitude. Here, the integration takes place from the level where the telescope is located to the border of the troposphere (generally 30 km). The atmospheric coherence length varies almost linearly with the wavelength of operation (precisely as $\lambda^{6/5}$) and inversely as C_n^2. In other terms, as turbulence increases, the value of atmospheric seeing increases while r_o decreases. For ground receiver sites, excellent values of seeing are around one half arcsec, with r_o larger than 20 cm for a wavelength of 500 nm.

As stated in the previous paragraph, the parameter C_n^2 indicates the turbulence of atmosphere and is derived by the structure function of the refractive index. In fact, in the hypothesis of statistically homogenous atmosphere, the refractive index structure function between two different points in space ($\mathbf{R_1}$ and $\mathbf{R_2}$) is

$$D_n(n(\mathbf{R})) \lesseqqgtr [n(\mathbf{R_1}) - n(\mathbf{R_2})]^2 \gtreqqless [n(\mathbf{R_1}) - n(\mathbf{R_1} + \mathbf{R})]^2 \geqq C_n^2 R^{2/3}$$

where $n(\mathbf{R_j})$ is the atmosphere refractive index (here a random variable) at $\mathbf{R_j}$, while $\mathbf{R}$ is the distance between $\mathbf{R_1}$ and $\mathbf{R_2}$ [17].

The structure index coefficient instead is greatly dependent on atmospheric parameters and in particular on pressure and temperature as

$$C_n^2 = \left(\frac{79 p}{T^2} \times 10^{-6} \right)^2 C_T^2$$

where the above equation also indicates that a way to determine the refraction index structure parameter is to measure temperature (T), pressure (p), and the structure coefficient of the temperature spatial fluctuations (C_T^2).

The equation clearly shows that the parameter C_n^2 can vary greatly due to variation of pressure and temperature, so the largest values of C_n^2 can be measured close to the ground where the continuous heating of the ground due to Sun illumination and the cooling during nighttime creates a temperature gradient with the surrounding atmosphere. A number of models are available in the literature for the profile of C_n^2 along the atmosphere. Here we describe three popular models — the CLEAR1, CLEAR2, and HV5/7 models. The CLEAR1 and CLEAR2 models were developed to describe the C_n^2 profile in the atmosphere at White Sands, New Mexico [18]. The CLEAR1 C_n^2 profile depends on the altitude as

$$C_n^2(h) = 10^{-17.025 - 4.3507h + 0.814h^2} f \; or \; 1.23 < h \leq 2.13 \text{ km}$$

$$C_n^2(h) = 10^{-16.2897 + 0.0335h - 0.0134h^2} f \; or \; 2.13 < h \leq 10.34 \text{ km}$$

$$C_n^2(h) = 10^{-17.0577 - 0.0449h - 0.00051h^2 + 0.618\exp(-05(h - 15.5617)/12.0173)} f \; or \; 10.34 < h \leq 30 \text{ km}$$

It must be noted that the CLEAR1 (and CLEAR2) models start at 1.23 km because this is the ground altitude at White Sands, which may be very appropriate to describe the high desert environment of the Goldstone location.

Concerning the HV5/7 model, this is a general model in closed form that is widely used in the field of adaptive optics and optical beam propagation in the turbulent atmosphere because it is relatively handy to treat with functions or mathematical derivations [19].

The name HV5/7 derives from the names of the individuals that first introduced the model (Hufnagel–Valley) and from the fact that the given parameters at the resulting atmospheric coherence length and isoplanatic angle (at 500 nm) are, respectively, 5 cm and 7 μm. The atmospheric refractive index structure constant profile according to the HV5/7 model can be written as

$$C_n^2(h) = 0.00594(21/27)^2 (10^{-5}h)^{10} \exp(-h/1000)$$
$$+ 2.7 \times 10^{-16} \exp(-h/1500) + 1.7 \times 10^{-14} \exp(-h/100)$$

where h is the altitude in meters.

The profile of C_n^2 according to CLEAR1, CLEAR2, and HV5/7 are illustrated in Figure 23, where all these curves show a common rapid decrement below the values at the ground layer, while the increment of C_n^2 at high altitudes is mainly due to the wind profile above 5 km.

The C_n^2 models represent an average distribution along the atmospheric profile derived from a number of measurements (CLEAR1 and CLEAR2) or an analytical model fitting the best of a number of different profiles (HV5/7). However, over the course of a day and at different locations, C_n^2 can greatly vary, and therefore a monitoring/measurement campaign is necessary to assess the characteristics of clear-air turbulence for the given site. A number of sensors/systems are used to characterize the profile of C_n^2 and/or the r_o. Specifically, a solar scintillometer [20] measures the daytime seeing by looking at the spatial fluctuations of the Sun irradiance, and the differential image motion monitor (DIMM) and the solar-DIMM [21] measure the seeing and r_o from the motion of the solar limb or of a star on
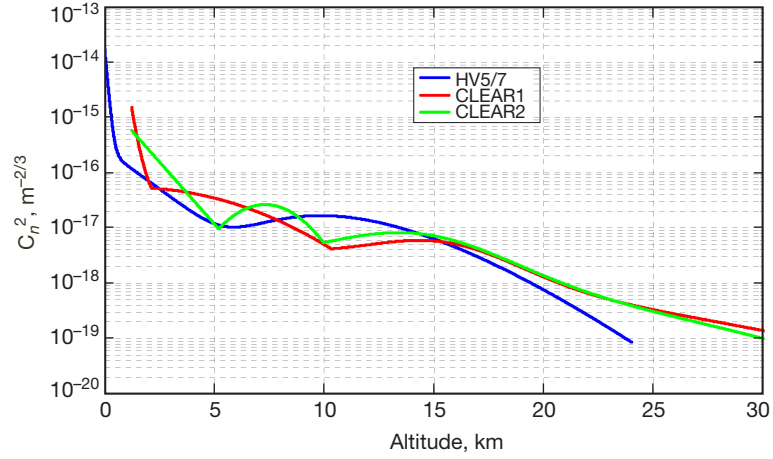
Figure 23. Refractive index structure coefficient profile of HV5/7, CLEAR1, and CLEAR2 models.

the focal plane of a charge-coupled device (CCD) camera. The multi-aperture scintillation sensor (MASS) [22] instead can profile the C_n^2 a different atmosphere layer using a reference star. These instrumentations are to be deployed in the near future. A first assessment of the clear-air turbulence was performed at Goldstone using a scintillometer to characterize the daily variation of the C_n^2 at the ground layer. The scintillometer used was the BLS900 from Scintec.[7] The BLS900 consisted of two transmitting discs composed of light-emitting diode (LED) emitters and a receiver. The transmitter was placed near the calibration tower at DSS-13, and the receiver of the BLS900 was placed on the roof of the transmitter building near the antenna itself — see Figure 24. The total pathlength measured was approximately 1500 m.
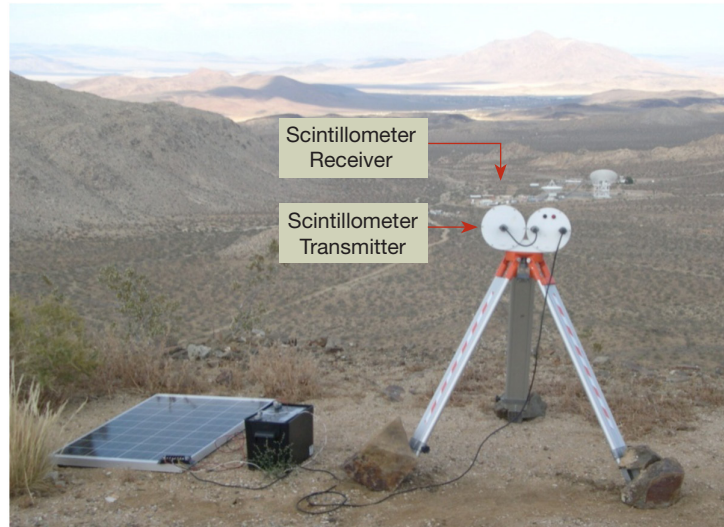

Figure 24. Scintillometer arrangement at Goldstone, DSS-13.

---

[7] http://www.scintec.com/

The fluctuation of power from the transmitter was measured by the receiver during operations over the course of six days (July 1 to July 7, 2009). As indicated by the theory, such fluctuation of signal, otherwise known as scintillation, is directly related to the refractive index structure coefficient [17]. Data from the measurements are indicated in Figure 25. According to the data, the variations of C_n^2 during the day have a well-established cycle. The peak is reached after noon where the refractive index structure index coefficient can reach values up to $4 \times E{-}14$ m$^{-2/3}$, and then there is a decrease where the lowest value of $2 \times E{-}16$ m$^{-2/3}$ is reached after sunset. The data also show that C_n^2 increases after sunset and stabilizes during the night, usually to reach a local minimum after dawn. The reason for these two daily minimum values is due to the fact that after sunset and around dawn there is a thermal equilibrium between the ground and the atmosphere, causing a reduction of the coefficient of the structure index of the temperature.
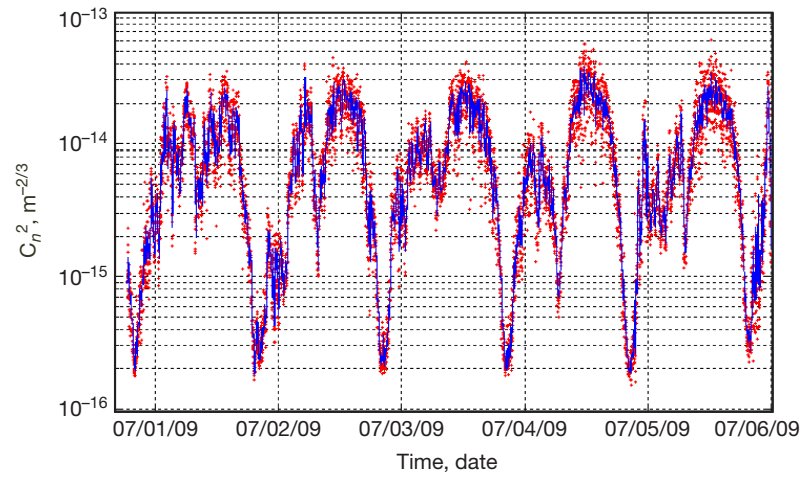

Figure 25. Measurement of the refractive index structure coefficient of the ground layer at Goldstone.

To derive an average daily plot of the variation of C_n^2, the data were averaged over a moving temporal window of 5 min. The results of these average daily variations are plotted in Figure 26 (solid curve). It can be noticed that C_n^2 still retains a minimum value after sunset. This is a remarkable result because, after time window averaging, the daily minimum values result in an overall (averaged) minimum of $8 \times E{-}16$ m$^{-2/3}$. Instead, it is difficult to distinguish the local minimum around dawn, which occurred at a different time for each day and contributed therefore to its partial disappearance when the daily data are averaged out. The maximum values of C_n^2, largest turbulence, always take place after noon, which is also reflected in Figure 26, where the curve indicates an average maximum value of circa $2 \times E{-}14$ m$^{-2/3}$.

Having measured the ground layer daily variation of the turbulence, a natural question is how to use the data to infer the possible values of the atmospheric coherence length at zenith. Without a proper sensor available to accomplish such a task, consideration was given to using a more practical method based on a multiplier, M, of profiles depicted in Figure 23.
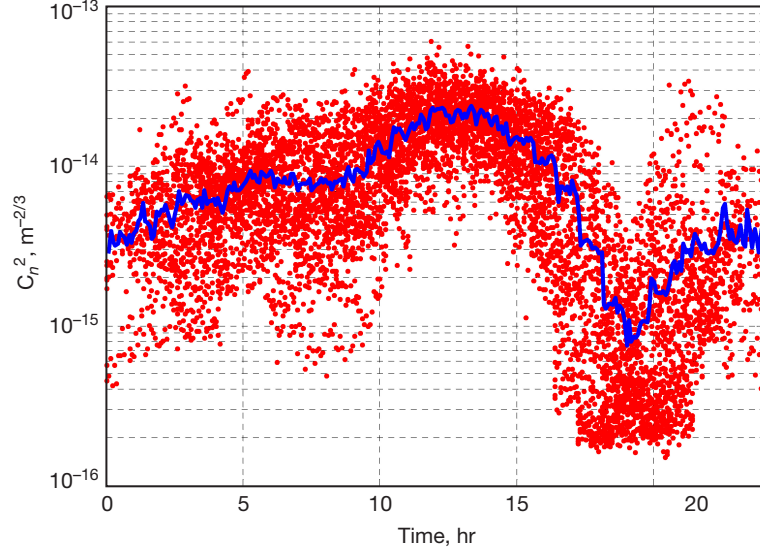
Figure 26. Daily variation of the ground layer of the refractive index structure coefficient at Goldstone. The average, blue curve, is over a temporal window of 5 min (solid curve). Instantaneous values are indicated by the spreading of the dots.

This multiplier multiplies the related profile — e.g., $C_n^2(h) = M \times \mathrm{HV}5/7(h)$ — and we then use this scaled profile to calculate r_o. To find M, one considers ground-measured values of C_n^2 and divides by the nominal profile's ground value. Of course, the multiplier will be a function of both measurement data set and model. By using this approach, we can obtain the daily variation of the atmospheric coherence length according to the HV5/7, CLEAR1, and CLEAR2 models. The results of this exercise are represented in Figures 27, 28, and 29, which show the daily variation of r_o according to the different models used. As is customary in astronomy, the wavelength used in calculating r_o was 500 nm.
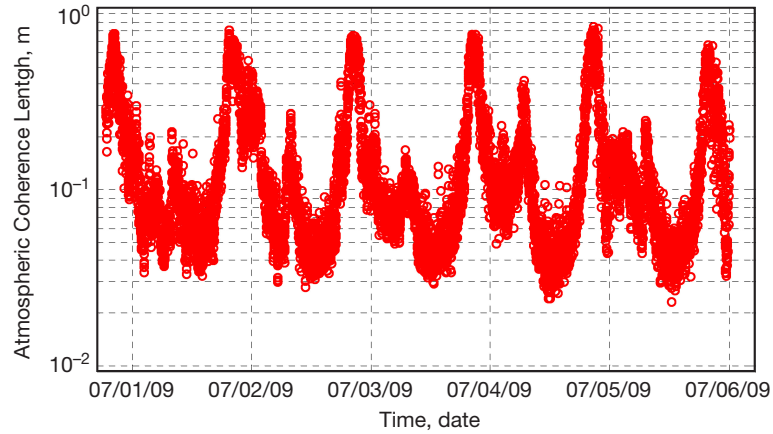

Figure 27. Temporal variation of the atmospheric coherence length at Goldstone using the HV5/7 model.
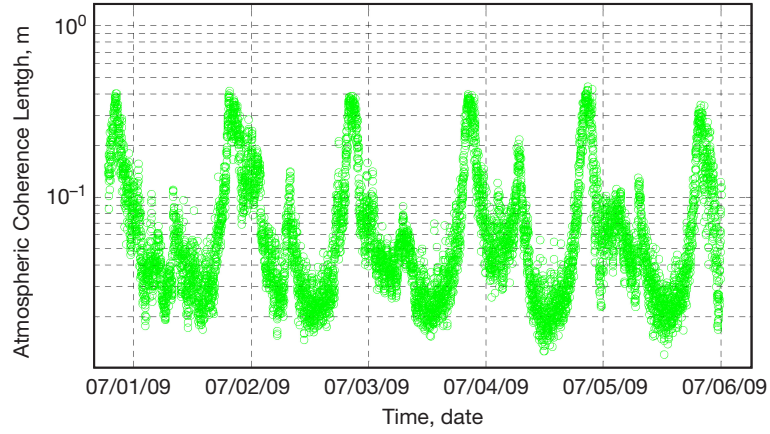
Figure 28. Temporal variation of the atmospheric coherence length at Goldstone using the CLEAR1 model.
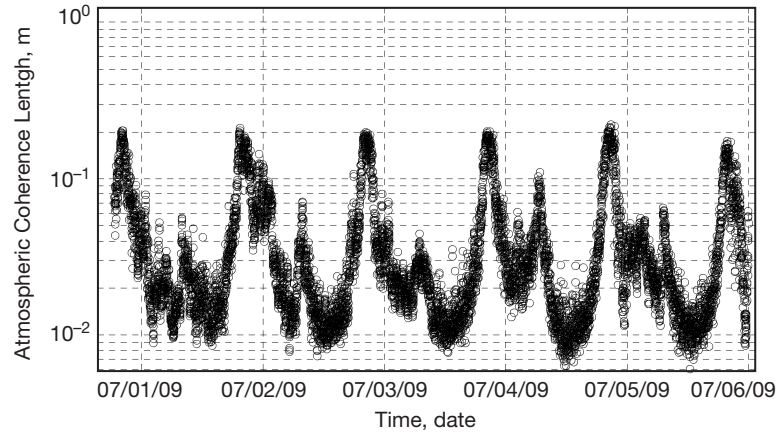

Figure 29. Temporal variation of the atmospheric coherence length at Goldstone using the CLEAR2 model.

Using the HV5/7 model, r_o values vary from a minimum of 2 cm to a maximum of 80 cm. Values of r_o as little as 2 cm can be expected for a desert environment such as Goldstone. However, general knowledge suggests that r_o is unlikely to be as large as 80 cm in an environment such as Goldstone. But by using the CLEAR1 and CLEAR2 models instead, values of r_o are much closer to what one may expect. In particular, CLEAR2, as plotted in Figure 29, indicates r_o, with a minimum of less than 1 cm occurring after noon and maximum value of 20 cm at sunset. CLEAR1 results, on the other hand (Figure 28) are between HV5/7 and CLEAR2, and most likely provide a better representation of the daily variation of the atmospheric coherence length at Goldstone.

Considering the daily variation of the atmospheric coherence length, we may derive the daily variation of the astronomical seeing according to the CLEAR1 and CLEAR2 models, as shown in Figure 30. Again, the CLEAR1 results seem most reasonable in providing the daily variation of the astronomical seeing at Goldstone, with instantaneous values varying from a minimum of 0.3 arcsec around sunset to 6 arcsec after noon. The average daily variation of the atmospheric coherence length, and of the astronomical seeing according
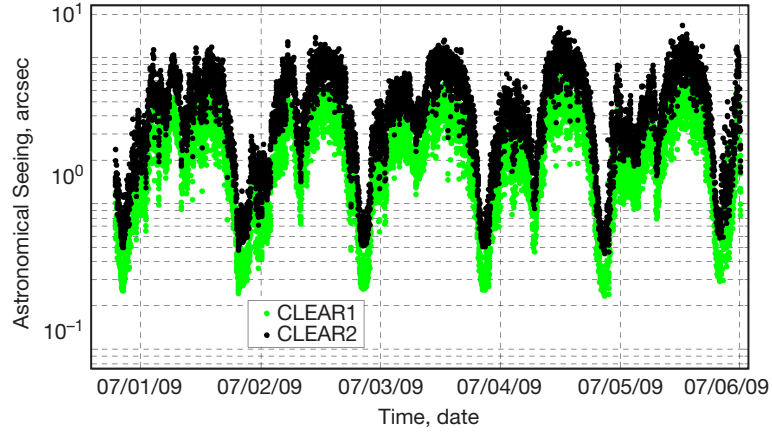
Figure 30. Temporal variation of the astronomical seeing at Goldstone according to CLEAR1 and CLEAR2 models. The astronomical seeing is indicated in arcsec.

to the CLEAR1 model approach, are depicted in Figures 31 and 32. As before, these average values were obtained using a moving temporal window of 5 min and the interpolation line is shown by the solid curve. Considering the astronomical seeing (Figure 32), one can notice that the worst condition (largest seeing) is around noon, with a seeing of 4.7 arcsec, while around sunset there is a minimum seeing of 0.7 arcsec. After sunset, the astronomical seeing rapidly degrades and during the night is in the range of 1.5 to 2.5 arcsec. After dawn, the (average) astronomical seeing remains constant, and when the boundary layer starts increasing in temperature (after hour 9), so does the value of astronomical seeing.

The availability of the (average) daily variation of the astronomical seeing is very important in the case of calculating the allowable data rates of a possible optical deep space link. In fact, the overall number of background photons captured by a receiver depends on the system field of view itself. This first evaluation of the daytime and nighttime seeing at Goldstone has produced results that are in good agreement with expectations for a desert environment at the appropriate altitude. However, a number of careful arguments must be made when using these values of atmospheric coherence length and astronomical seeing derived here for Goldstone. First, these data are obtained only by using the measurements of the ground layer. It will be necessary in the future to validate these data by measuring directly the r_o and astronomical seeing. These measurements will be performed in this coming year. Next, these data refer to just a week of measurements during the summer. At the same time, clear-air turbulences greatly depend on the Sun daily cycle; therefore, it is important to extend the measurements to larger periods and different periods and seasons of the year.

VIII. Conclusions and Future Work

The first phase of a study of the concept of combining the existing 34-m RF ground terminal with a new 10-m-class optical terminal has been completed. Here we have discussed in some detail many of the unique issues that must be addressed in the design of the combined terminal. These include operation in an open-air environment, acquisition and
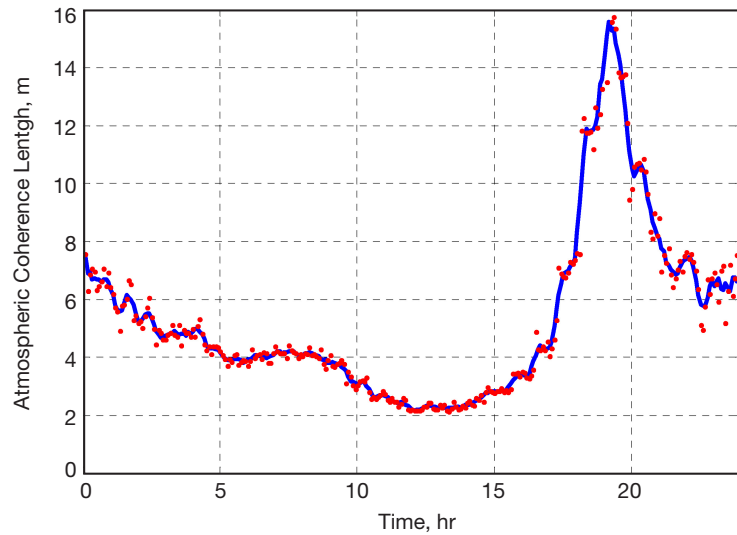
Figure 31. Daily variation of atmospheric coherence length at Goldstone. The data are obtained by time averaging over a temporal window of 5 min. The blue curve is the interpolation line among the data set (red dots).
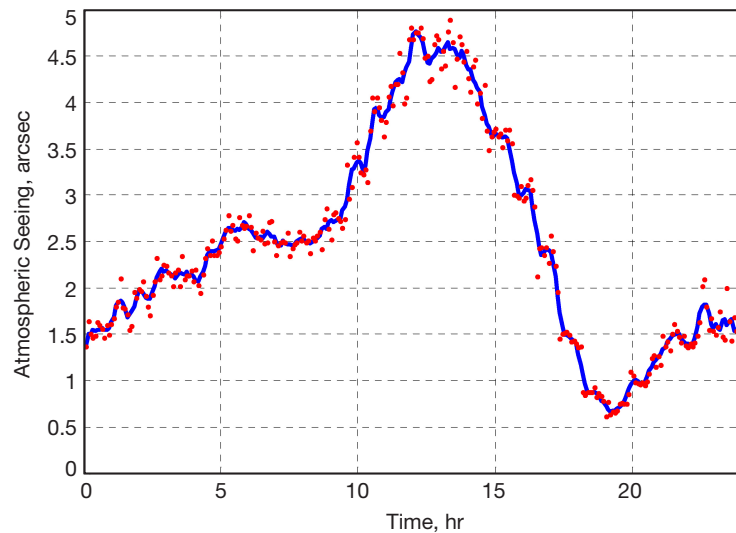

Figure 32. Daily variation of astronomical seeing at Goldstone. The data are obtained by time averaging over a temporal window of 5 min. The blue curve is the interpolation line among the data set (red dots).

tracking, separation of the RF and optical signals, impact of the optical components on the RF performance, and unique factors in the optical design that are required for this application. A combination of sample measurements, field measurements, and calculations has been completed in order to quantify many effects. These data were then used as input to the strawman design process. We have also reported some preliminary results on the Goldstone optical communication environment, including daytime operating conditions.

Problems associated with signal separation, RF/optical refraction effects, and dual-use mirror coatings appear to be solvable. Contamination rates at Goldstone have been quantified, but mirror contamination remains a significant factor, likely requiring very frequent cleaning

for small SEP angle tracking. Existing surface distortions due to gravity effects have been quantified and folded into current FSM and/or detector field of view considerations. Preliminary measurements of daytime seeing and associated atmospheric coherence length at Goldstone are in good agreement with published data for a desert environment.

There are still many technical challenges for the combined terminal that remain unstudied. Future work will focus on stray light analysis and structural aspects of the design. The structural analysis will include changes required to accommodate the additional weight of the optical surfaces and components, and provide a first-order cost estimate for the changes required. Further work is also required on the acquisition and tracking problem and more detailed analysis of the RF and optical surface profiles for the shared-aperture design is also planned. Additional testing would also be valuable. For example, optic and optical material weathering and cleaning tests should be conducted. Upon completion of these preliminary design tasks, we will be in a position to properly assess the viability of the combined terminal in terms of performance, operational constraints, and to some extent, implementation and operational costs.

References

[1] H. Hemmati, *Deep Space Optical Communications*, JPL Deep-Space Communications and Navigation Series, New Jersey: Wiley & Sons, Inc., 2006.

[2] J. Eite and A. G. Spencer, "Indium Tin Oxide for Transparent EMC Shielding and Anti-static Applications," presentation at the *EMC Exhibition and Conference* (EMCUK), Newbury, UK, 2004.

[3] B. G. Patrick, P. Gierow, D. Sheikh, and W. T. Roberts, "Solar Filter for the Mars Laser Communication Demonstration Optical Receiver, *Proceedings of SPIE,* vol. 5550, pp. 336–343, October 20, 2004.

[4] D. M. Boroson, A. Biswas, and B. L. Edwards, "MLCD: Overview of NASA's Mars Laser Communications Demonstration System, *Proceedings of SPIE*, vol. 5338, pp. 16–28, July 7, 2004.

[5] M. D. Britcliffe, D. Hoppe, W. Roberts, and N. Page, "A Ten-Meter Ground-Station Telescope for Deep-Space Optical Communications: A Preliminary Design," *The Interplanetary Network Progress Report*, vol. 42-147, Jet Propulsion Laboratory, Pasadena, California, pp. 1–17, July-September 2001, article dated November 15, 2001. http://ipnpr.jpl.nasa.gov/progress_report/42-147/147G.pdf

[6] E. Roache, R. Irvin, and J. S. Perkins, "Mirror Facets for the VERITAS Telescopes," *Proceedings of the 30th International Cosmic Ray Conference*, Mérida, Yucatán, Mexico, July 3–11, 2007, vol. 3, pp. 1397–1400, published 2008.

[7] P. R. Spyak and W. L. Wolfe, "Scatter from Particulate-Contaminated Mirrors," *Optical Engineering*, vol. 31, no. 8, pp. 1746–1784, August 1992.

[8] J. R. Varsik, W. Siegmund, and D. H. Berger, "Telescope Mirror Contamination and Airborne Dust," *Bulletin of the American Astronomical Society*, vol. 29, p. 898, May 1997.

[9] C. I. Calle, C. R. Buhler, J. L. McFall, and S. J. Snyder, "Particle Removal by Electrostatic and Dielectrophoretic Forces for Dust Control during Lunar Exploration Missions," *Journal of Electrostatics*, vol. 67, issues 2–3, pp. 89–92, May 2009 (11th International Conference on Electrostatics, Valencia, Spain, May 27–29, 2009).

[10] M. J. Britcliffe and R. C. Clauss, "The Effects of Water on the Noise-Temperature Contribution of Deep Space Network Microwave Feed Components, *The Telecommunications and Data Acquisition Progress Report*, vol. 42-145, Jet Propulsion Laboratory, Pasadena, California, pp. 1–5, January–March 2001, article dated May 15, 2001.
http://ipnpr.jpl.nasa.gov/progress_report/42-145/145G.pdf

[11] M. A. Gudim, W. Gawaronski, W. J. Hurd, P. R. Brown, and D. M. Strain, "Design and Performance of the Monopulse Pointing System of the DSN 34-Meter Beam-Waveguide Antennas," *The Telecommunications and Mission Operations Progress Report*, vol. 42-138, Jet Propulsion Laboratory, Pasadena, California, pp. 1–29, April–June 1999, article dated August 15, 1999.
http://ipnpr.jpl.nasa.gov/progress_report/42-138/138H.pdf

[12] I. M. Perez-Borroto and L. S. Alvarez, "Atmospheric Refraction Correction for Ka-Band Blind Pointing on the DSS-13 Beam-Waveguide Antenna," *The Telecommunications and Data Acquisition Progress Report*, vol. 42-111, Jet Propulsion Laboratory, Pasadena, California, pp. 62–70, July–September 1992, article dated November 15, 1992.
http://ipnpr.jpl.nasa.gov/progress_report/42-111/111F.PDF

[13] Nautical Almanac Office (U. S.), *The Astronomical Almanac for The Year 2009*, p. B87, Washington, DC: U. S. Government Printing Office, 2008.

[14] W. A. Imbriale, M. J. Britcliffe, and M. Brenner, "Gravity Deformation Measurements of NASA's Deep Space Network 70-Meter Reflector Antennas," *The Interplanetary Network Progress Report*, vol. 42-147, Jet Propulsion Laboratory, Pasadena, California, pp. 1–15, November 15, 2001.
http://ipnpr.jpl.nasa.gov/progress_report/42-147/147I.pdf

[15] B. N. Holben, T. F. Eck, I. Slutsker, D. Tanré, J. P. Buis, A. Setzer, E. Vermote, J. A. Reagan, Y. J. Kaufman, T. Nakajima, F. Lavenu, I. Jankowiak, and A. Smirnov, "AERONET — A Federated Instrument Network and Data Archive for Aerosol Characterization," *Remote Sensing of Environment*, vol. 66, issue 1, pp. 1–16, October 1998.

[16] D. L. Fried, "Optical Resolution through a Randomly Inhomogeneous Medium for Very Long and Very Short Exposures," *Journal of the Optical Society of America*, vol. 56, issue 10, pp. 1372–1379, 1966.

[17] V. I. Tatarskii, *The Effects of the Turbulent Atmosphere on Wave Propagation*, Israel Program for Scientific Translations, reproduced by National Technical Information Service, U. S. Department of Commerce (published for NOAA), Jerusalem and Springfield, Virginia, 1971.

[18] R. R. Beland, "Propagation through Atmospheric Optical Turbulence," Chapter 2 in Frederick G. Smith, ed.: *The Infrared and Electro-Optical Systems Handbook, Vol. 2*: Bellingham, Washington: SPIE Optical Engineering Press, 1993.

[19] L. C. Andrews and R. L. Phillips, *Laser Beam Propagation through Random Media*, Bellingham, Washington: SPIE Optical Engineering Press, 1998.

[20] E. J. Seykora, "Solar Scintillation and the Monitoring of Solar Seeing, *Solar Physics*, vol. 145, no. 2, pp. 389–397, 1993.

[21] J. M. Beckers, "A Seeing Monitor for Solar and Other Extended Object Observations, *Experimental Astronomy*, vol. 12, no. 1, pp. 1–20, January 2001.

[22] V. Kornilov, A. A. Tokovinin, O. Vozyakova, A. Zaitsev, N. Shatsky, S. F. Potanin, and Marc S. Sarazin, "MASS: a Monitor of the Vertical Turbulence Distribution," *Proceedings of SPIE, Adaptive Optical System Technologies II Conference*, August 22, 2002, Waikoloa, Hawai'i, vol. 4839, pp. 83–845, published 2003.